The Thesis Committee for Andre Gouws
Certifies that this is the approved version of the following Thesis:

Initial Stage Selective Laser Flash Sintering of Aluminum Nitride

APPROVED BY
SUPERVISING COMMITTEE:

Desiderio Kovar, Supervisor

Joseph J. Beaman, Co-Supervisor

Initial Stage Selective Laser Flash Sintering of Aluminum Nitride

by

Andre Gouws

Thesis

Presented to the Faculty of the Graduate School of

The University of Texas at Austin

in Partial Fulfillment

of the Requirements

for the Degree of

Master of Science in Engineering

The University of Texas at Austin

May 2020

To my family with love

Acknowledgements

We gratefully acknowledge support from the Office of Naval Research under the direction of Dr. Antti Makinen (grant number N00014-18-1-2261). We also thank Mr. Jeremiah McCallister for his assistance in imaging the AlN powder in TEM. The support of the U.S. Department of Energy, Office of Nuclear Energy Nuclear Technology Research and Development program is gratefully acknowledged. Part of this work was performed at Los Alamos National Laboratory which is operated by Triad National Security, LLC, for the National Nuclear Security Administration of the U.S. Department of Energy under contract number 89233218CNA000001.

Abstract

Initial Stage Selective Laser Flash Sintering of Aluminum Nitride

Andre Gouws, M.S.E.

The University of Texas at Austin, 2020

Supervisor: Desiderio Kovar

Co-Supervisor: Joseph J Beaman

Flash sintering is a form of sintering where electric fields are combined with heating to reduce the time and temperature required to densify ceramic powder compacts. A previous study with yttria-stabilized zirconia has shown that selective laser flash sintering (SLFS) is possible in which a scanning laser is used to selectively flash sinter a local region of the sample. SLFS presents the opportunity to avoid many of the drawbacks of current indirect additive manufacturing methods that utilize a binder. In this work, we demonstrate that aluminum nitride can also undergo SLFS using a combination of measurements of electric current flowing through the sample and observations of necks formed between powder particles. The scan conditions required to initiate SLFS are characterized over a range of laser powers and laser scan speeds. It is shown that the initiation of SLFS in AlN is governed by both the local heat input and heat dissipation. A numerical model that accounts for heat input using the product of the power intensity and laser interaction time and heat dissipation from conduction, convection, and radiation is developed. This model suggests that, consistent with furnace-based flash sintering, a minimum temperature along the conductive path determines the onset of sintering. Under an applied field of 3000 V/cm, temperatures of 450 – 475 K are predicted to initiate SLFS in AlN in 1.25 – 0.25 s. A second model is developed to determine the characteristics of sintering at the micro-scale for various combinations of heating and electrical fields, and particle geometries. This

model suggests that the time to the onset of flash sintering is strongly dependent on the applied laser heating for the range of electric fields typically applied in SLFS. It also suggests that the time to the onset of SLFS is less dependent on electric field, but that after flash initiates the field strongly effect the temperature in the scanned region of the sample.

Table of Contents

List of Tables

List of Figures

CHAPTER I: INTRODUCTION AND MOTIVATION

1. Introduction to Sintering

1.1. Conventional Sintering of Ceramics

Unlike polymers and metals which are usually processed using melt processes, the very high melting temperatures of most ceramics requires processing methods that do not require melting. Ceramic processing conventionally begins with forming, where powder is either physically pressed, mixed with liquids to produce a mass that can be shaped, or cast from a slurry (1). Following the forming process, the parts are referred to as "green" parts. The green parts may contain polymer additives that remain from the forming process and these are removed by a low temperature heat treatment in which any remaining polymer additives are pyrolyzed. The parts following pyrolysis typically contain 40-50% porosity and are very fragile. To increase the densify the parts and increases their strength, they sintered by exposing them to temperatures of between 50-90% of the melting temperature for several hours. The high temperatures and long times used during conventional sintering processes result in significant grain growth regardless of initial particle size (2). The long times and high temperatures can both be reduced by applying an pressure as an additional driving force to consolidate the powders (hot isostatic pressing), but this process is prohibitively expensive for mass production and limits part geometries.

1.2 Electric-Field Assisted Sintering

It has been shown that sintering times and temperatures can also be reduced by applying an electric field to the sample during sintering. Two notable forms of sintering using electric fields are Spark Plasma Sintering (SPS) and Flash Sintering (FS). SPS is a process where ceramic powder is surrounded with a graphite die, and electric current is

passed through the die to heat it via joule heating. This heated die then transfer the heat to the powder to cause sintering to occur.

Flash sintering uses a combination of external heating from a furnace and a large electric field to consolidate the part. Because ceramics have lower electrical conductivity than materials such as graphite, flash sintering often requires higher voltages and activation energies than SPS. Flash sintering was first discovered by Cologna *et al.* (3), and has subsequently been used on a large number of different ceramic materials by applying fields of between 7.5 V/cm – 3000 V/cm and power dissipations of between 10 – 1000 mW/mm^3 (4,5,6) It has been shown that Flash sintering initiates in a ceramic after a certain threshold external temperature and electric field are reached, after which conductivity of the ceramic increases and it becomes conductive (8). Many different mechanisms have been proposed to explain how flash sintering works, including bulk and local joule heating, (8,10) the formation of Frenkel defects (4,15), and electrochemical reduction (7).

1.3 MECHANISMS OF FLASH SINTERING

The first mechanism proposed to explain flash sintering was proposed by Todd *et al.* (8) They suggested that flash sintering results from rapid bulk heating of a ceramic material due to Joule heating. The theory of Joule heating as a driver for flash sintering rests on the assumption that Joule heating drives very high temperatures far beyond the initial onset temperature within an incredibly short length of time, resulting in the power density needed to sintering the material within a very short time scale. (9,10) It has been shown that temperatures within flashed ceramics such as 8YSZ rise approximately 1000 C° above the onset temperature for flash, therefore providing enough energy for densification to take place within 15 sec (11).

Another mechanism to explain flash sintering was proposed by Cologna *et al.* that proposes that localized heating at grain boundaries is responsible for the flash effect. (3) They suggest that high temperature gradients and high local temperatures at particle contact points result in joule heating at these connection points. This is in contrast to the proposed mechanism of bulk joule heating across the entire material as originally proposed by Todd *et al.* Chaim (12) has proposed that these local effects are so prevalent, that melting occurs at the particle contacts and that resulting capillary forces aid the densification of powders during flash sintering. In addition, since the liquid conductivity for materials is typically higher than the solid conductivity, this could contribute to rapid thermal runaway.

Raj *et al.* (3) has proposed an alternative mechanism that suggests that the nucleation of defects known as Frenkel pairs are the driving mechanism for flash sintering. A Frenkel pair are point defects that consist of a vacancy and interstitial ion, that due to their opposite charges, are closely coupled. Their theory proposes that an avalanche of Frenkel pairs are formed due to the combination of field and high temperatures that result in a greatly enhanced rate of mass transport. However, Frenkel pair formation does not explain incubation times that were observed by Naik *et al.* (13)

Another theory that has been proposed is that flash sintering in ionic conductors can be explained by an induced electrochemical reduction (14). It is proposed that the voltage applied to the sample to produce the electric field in flash sintering can exceed the electrochemical reduction potential for an ionic conductor. If this occurs, the material transitions from an insulator to an electronic conductor. (14) This mechanism the observed incubation stage, (14,15) which is explained by electrochemical reduction progressing from anode to cathode, and the flash event itself. (3)

1.4 Additive Manufacturing of Ceramics

Ceramic Additive Manufacturing (AM) consists of a new multitude of manufacturing methods designed to additively manufacture ceramic materials in a layer-by-layer process. Ceramic AM processes can be categorized as either direct (single step) or indirect (multi step) processes (16). Direct processes allow for the shaping and final material properties to be achieved simultaneously, while indirect processes require a step that first achieves the geometry and then at least one additional stage where the part is consolidated to the final material properties.

Direct additive manufacturing presents significant challenges because the sintering times for ceramics is typically hours for typical sintering temperatures, as discussed in Section 1.1 (17). The sintering time can, in principle, be decreased by increasing the temperature. However, to achieve sintering in the short time a localized heat source passes over a surface in AM, the sintering times must be reduced to the fractions of a second. The very high temperatures required to achieve such fast sintering typically results in thermal shock cracking because of the severe temperature gradients and the low fracture toughness of most ceramics (18). Thus, direct AM processes cannot be used with most ceramics.

There are several different indirect additive manufacturing routes that have been successfully demonstrated for the production of ceramics including selective laser sintering (SLS) (19), stereolithography (SLA) (20), binder jetting (21), and fused deposition modeling (FDM). For each of these indirect additive manufacturing routes (see Fig. 1.1), a ceramic powder is mixed with a polymer binder. The polymer/ceramic blends behave similarly to neat polymer and thus the green part can be 3D printed using machine parameters and temperatures that are modified slightly relative to printing neat polymers (**Error! Bookmark not defined.**). Following this, the binder must be removed via pyrolysis, and then the remaining ceramic part is sintered. One challenge with indirect AM

is that the decomposition products from binder must escape without distorting or cracking the part. In practice, this can only be achieved for thin-walled or small parts that are heated slowly. Thus, there remains a need for an AM processes that is capable of producing large or thick-walled parts.

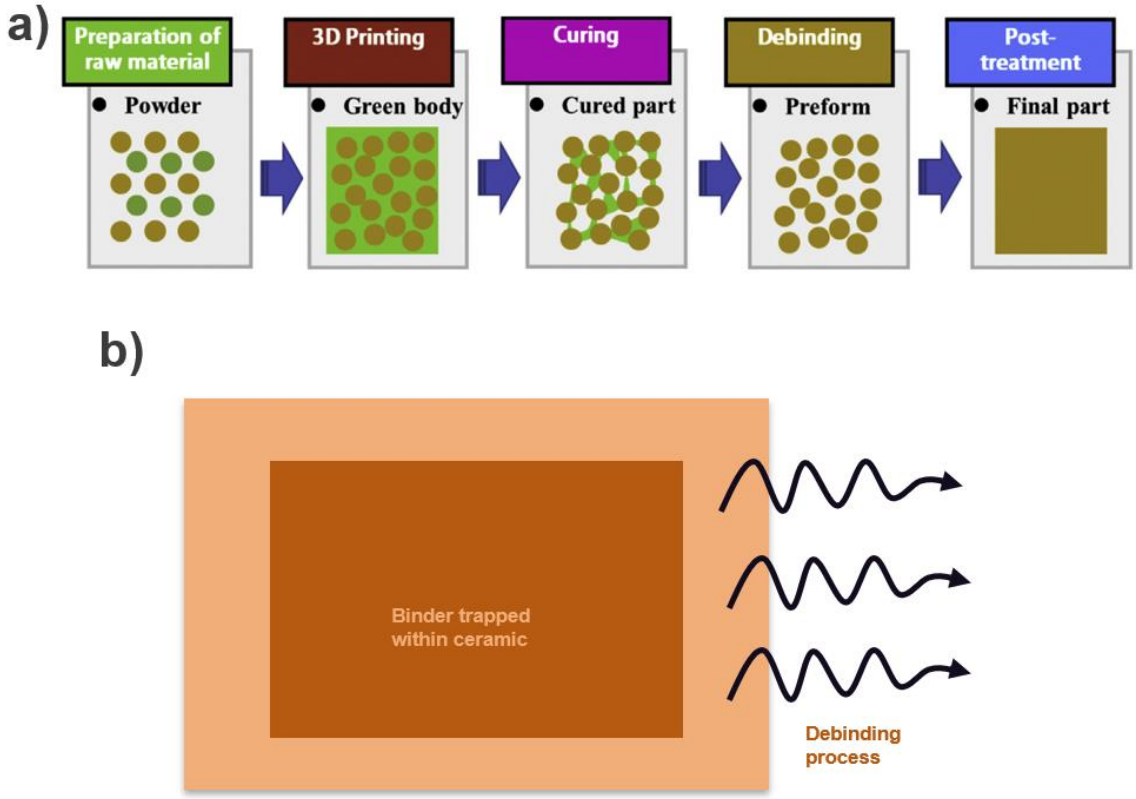

Figure 1.1: a) The five-step process for indirect additive manufacturing of ceramics, and b) the debinding process by which the binder is removed from the ceramic Courtesy Lv *et. al.* (22)

2. Selective Laser Flash Sintering

Selective Laser Flash Sintering (SLFS) is a form of flash sintering where ceramic is heated by selective heating using a laser rather than furnace-based heating. In the SLFS process, compacted powder is placed between two electrodes and heat deposited via a laser travelling across the sample surface. The combination of laser heating and electric field results in sintering within the heated region of the sample. Figure 1.2 shows the differences between SPS (Fig. 1.2a), conventional flash sintering (Fig. 1.2b), and SLFS (Fig 1.2c).

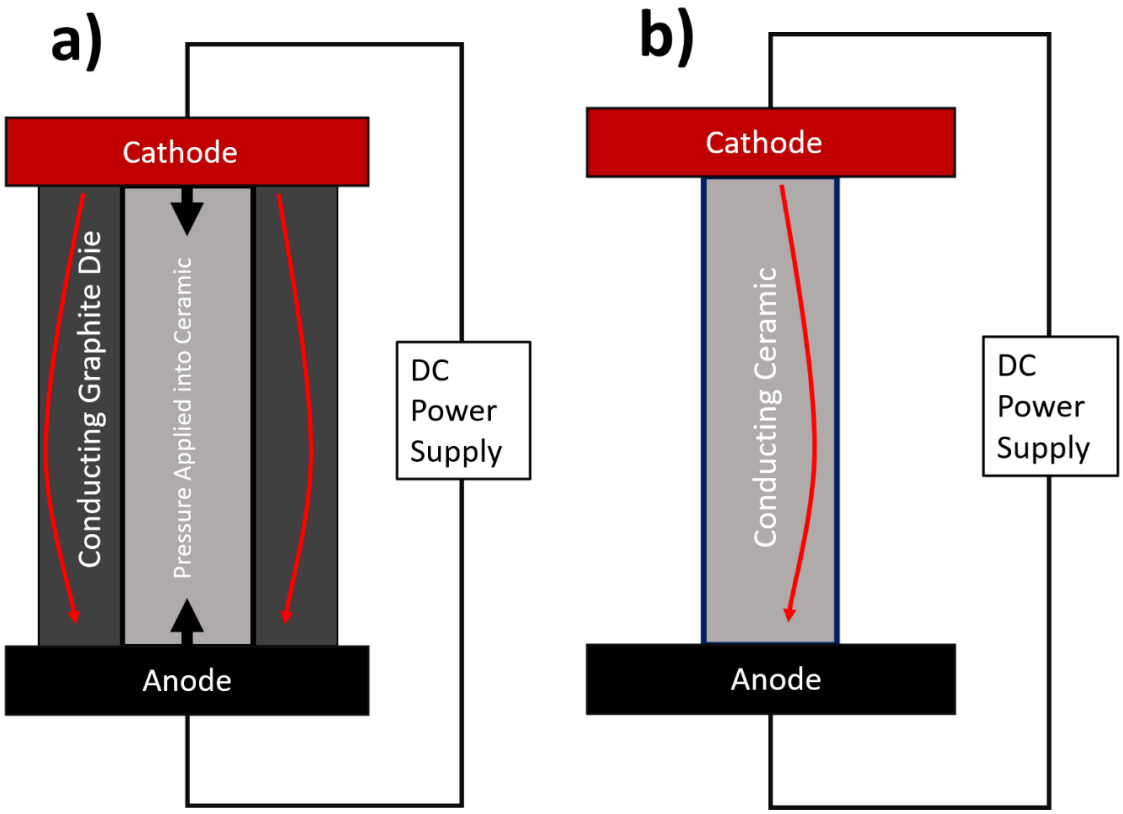

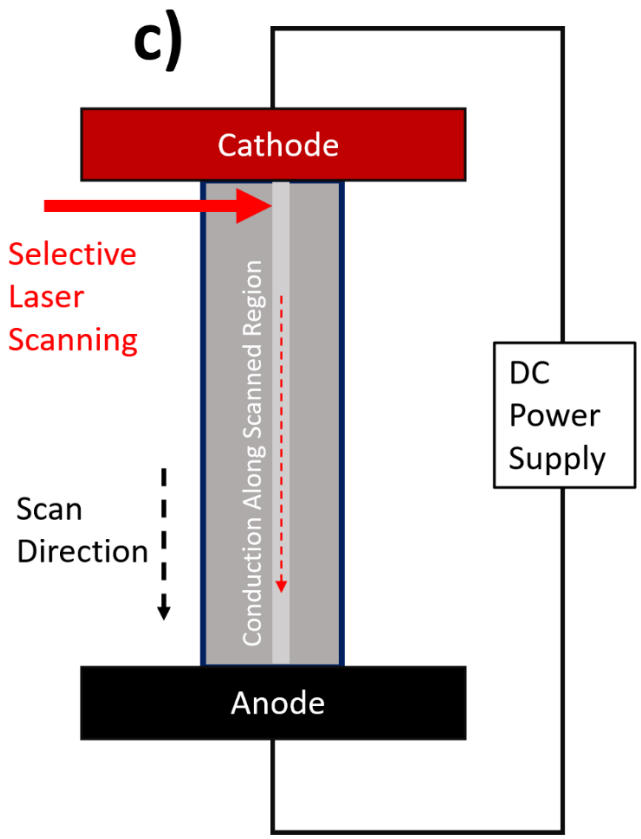

Figure 1.2: The processes of a) spark plasma sintering, b) conventional flash sintering, and c) Selective Laser Flash Sintering

SLFS may offer an opportunity to overcome the major drawbacks of existing direct and indirect AM processes for the additive manufacture of ceramics. To overcome the challenges of direct AM, it is necessary to avoid cracking. SLFS enables this in three important ways: 1) The presence of the electric field decreases the sintering temperature by several hundred degrees relative to furnace-based sintering, 2) The presence of the electric field decreases the sintering time to fractions of a second and 3) The sintering conditions can be set to allow only the onset of SLFS so that necks form between the particles (see Fig. 1.3) to hold the part together, but the part does not fully densify. By

only partially sintering the part, the sintering time and temperatures can both be reduced and porous ceramic are more resistant to large thermal gradients (23).

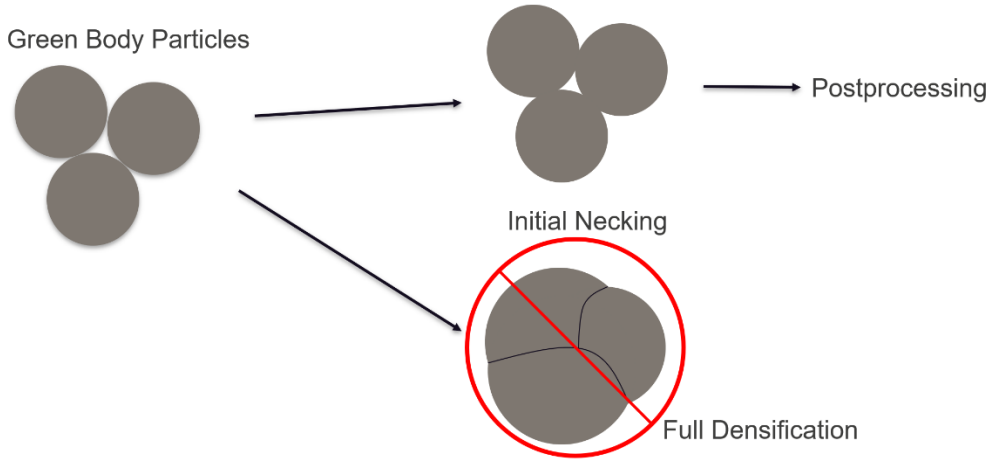

Figure 1.1: The goal of the SLFS process is to only partially create necks in the samples, and then subject them to postprocessing for full densification – not to fully densify them entirely with SLFS

To implement SLFS as a multi-layer additive manufacturing process, it will likely be necessary to form each layers of material just before scanning. Deborah Hagen has demonstrated this approach (ref. unpublished work) using a tapecasting approach. A slurry is first produced consisting of the ceramic powder, polymer binder, and a solvent. The slurry is then tapecast into a thin layer on the part bed. The laser is then scanned over the regions of interest at low powers to remove the binder and then rescanned over these regions to partially sinter them. This process is repeated until the green part is completed. The part is then placed in a solvent to dissolve the polymer in the unscanned regions; the scanned regions remain intact because of the particle necks between the particles. The remaining part is then placed in a furnace and conventionally sintered. Compared to other indirect AM processes for producing ceramics, multilayer SLFS offers the advantage of

not requiring a pyrolysis step on the green part because the polymer is removed layer by layer as the part is being built. Thus, thick walled and large bulk parts should be possible.

To further develop the SLFS process, it is important to understand the various controlling parameters and how they affect the properties of final parts. Previously, Hagen (30) successfully demonstrated the ability to SLFS yttria-stabilized zirconia. In addition, the effects of laser power, electric field, and moisture on samples were characterized. Yttra-stabilized zirconia is a material which has been extensively studied in the conventional flash sintering literature before (3,24,25) and provides an important benchmark for further characterization of the SLFS process. To date, flash sintering and SLFS have not been demonstrated on any nitride-based ceramics. AlN is an interesting candidate ceramic for SLFS because it has extremely high thermal conductivity (40) which makes it an attractive candidate for nuclear applications where heat must be dissipated effectively. The goal of this work is to expand the understanding of SLFS by characterizing the parameters needed to initiate SLFS of aluminum nitride and understand the microscale mechanics of the SLFS process.

CHAPTER 2: INITIAL STAGE SELECTIVE LASER FLASH SINTERING OF ALUMINUM NITRIDE

2.1 Introduction

Flash sintering is method for rapidly sintering ceramics that utilizes the simultaneous application of heat and an electric field (26,27). Flash sintering initiates when a threshold temperature and electric field are exceeded and is characterized by the onset of measurable electric current through the part. (28) During this initial stage of flash sintering, there is neck growth between powder particles, but minimal densification and the only a small current flow through the sample. (29) During second stage flash sintering, densification occurs as the current increases rapidly. To avoid current runaway, during third stage flash sintering, the power supply is switched from voltage control to current control and further densification and coarsening occur.

Because the flash sintering phenomenon can occur quickly and at a much lower temperature than conventional sintering, a scanning laser can be used as a heat source to selectively sinter parts of the sample using a process called selective laser flash sintering (SLFS). The SLFS process has been previously demonstrated using 8%mol yttria-stabilized zirconia (8-YSZ). (30) It was shown that a combination of laser heating and electric field could be used to initiate flash sintering, and that densification could be controlled by adjusting the laser power and electric field strength. Although SLFS has not yet been demonstrated on any other ceramics to date, a large number of oxide (31,32) and carbide ceramics (33,34) have previously been conventionally flash sintered using a furnace, suggesting that other ceramics may be candidates for SLFS. Aluminum nitride

presents an opportunity to discern the limits of the SLFS process, because it has a similar bandgap to 8-YSZ but two orders of magnitude greater thermal conductivity. Because the flash process is known to be temperature-dependent, thermal conductivity is expected to have a significant effect on the initiation of the SLFS process. In this paper, the conditions required to initiate SLFS are studied and related to processing conditions and material properties. The focus is on characterizing the first stage of SLFS, where the current flow through the sample first begins. It is shown that in high conductivity ceramics such as AlN, both heat input as well as heat transfer must be tracked to determine the conditions required for the onset of SLFS.

2.2 Experimental Procedure

Commercial AlN powder (Grade C Aluminum Nitride, HC Starck, Karlsruhe, Germany) with a particle size of between 0.8 – 2.0 μm was uniaxially pressed using 2.54 cm steel, cylindrical dies, that were lubricated using a 2% steric acid/acetone solution. The resulting pellets were approximately 3.5 – 4.0 mm thick and had a green density of 1.4 g/cm^3. Colloidal silver (PELCO, Ted Pella, Redding, CA) was used to create two electrically conductive regions on opposite sides of the face of the pellet. The pellets were heated in an oven at 125˚C for one hour prior to testing to remove adsorbed moisture since previous experiments have shown that moisture may affect the conditions required to initiate SLFS (35).

Schematics showing the SLFS apparatus and specimen geometry are shown in Fig. 2.1. Figure 2.1a shows the configuration of the green, AlN pellet placed on top of an

insulator between two steel electrodes. Copper tape was used to connect the painted silver electrodes on the sample to the steel electrodes. A chamber was placed over the sample to allow the sample to be purged with dry N_2 for 2 minutes to exclude moisture and oxygen. A voltage was applied between the electrodes using a high voltage power supply (PS350, Standard Research Systems Inc., Sunnyvale, CA) to generate the electric field across the sample. The electric field applied to the pellets was varied from 0 – 3000 V/cm. Current conducted through the sample during the experiment was measured with a precision of 1 μA at a frequency of 500 Hz using a data acquisition system (CompactRIO, National Instruments, Austin, TX).

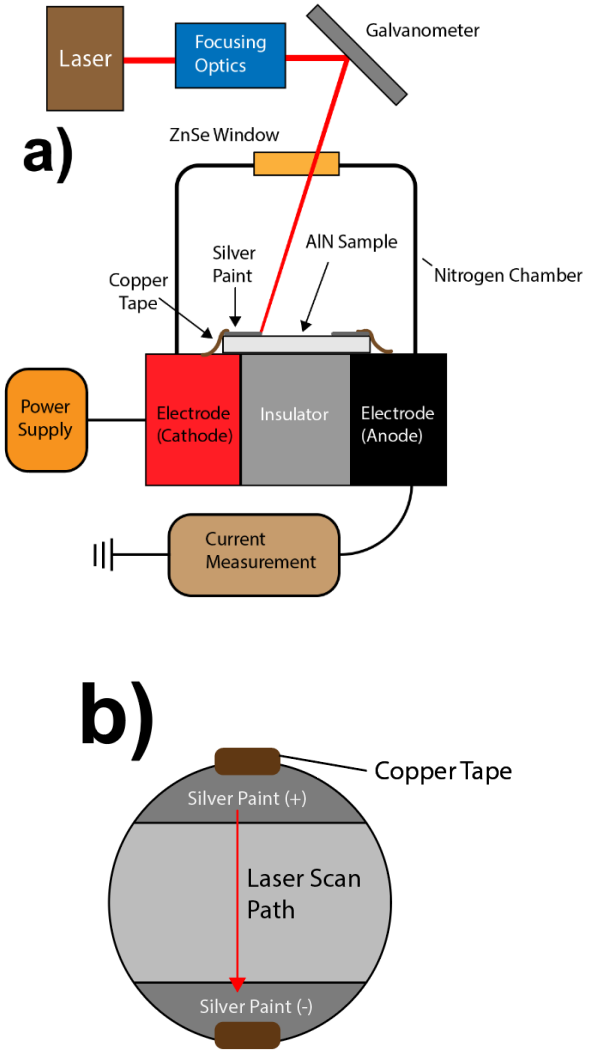

Figure 2.1 The selective laser flash sintering (SLFS) experimental setup: a) Schematic showing an overview of the experimental apparatus and b) plan-view of the specimen and electrode geometries.

The only source of heat on the sample was from a focused, continuous wave CO_2 laser that was scanned across the pellet surface. The wavelength of the laser was 10.6 μm and it had a maximum rated power of 55 W (48-5, SYNDRAD, Mukilteo, WA). A pair of mirror galvanometers (6240H, Cambridge Technology, Bedford, MA) were used to scan the beam through a zinc selenide window mounted on the top chamber and across the pellet surface. The profile of the beam on the specimen surface had a gaussian distribution with a full width at half maximum of approximately 350 – 400 μm.

Figure 2.1b shows details of the specimen and laser scan pattern in plan-view. For all of the experiments conducted in this study, the laser was scanned in one dimension from the cathode to the anode at velocities of 33 – 300 mm/s and laser powers of 10 – 30 W (3×10^{-5} – 6×10^{-5} J/mm^2) on the sample surface. A total of 8 – 10 parallel line paths, separated by a distance of 2.5 mm, were scanned on each pellet surface. For most experiments, each line path was repeatedly scanned over the same path up to 20 times. When repeated scans were conducted on the same line path, the laser was first activated with the beam on the cathode. The scan then commenced across the sample surface and then onto the anode, where the laser was shut off. The beam was then repositioned onto the cathode before turning the laser back on and repeating the scan. Approximately 10 ms transpired from the completion of one scan before the next scan on the same line path commenced. Scanning of the next parallel line path was delayed for at least XX seconds to ensure that the pellet had returned to a temperature near room temperature before scanning the next line path. Upon completion of the experiments, the surfaces of the samples were sputter-coated with

conducting Au-Pd so that they could be imaged using a scanning electron microscope (Vega 3, Tescan-Orsay, Brno, Czech Republic) in secondary electron imaging mode.

2.3 Experimental Results

Figure 2.2a shows the current measured through the pellet versus the laser scan time for a scan speed of 100 mm/s, laser power of 20 W, an electric field of 0 V/cm. For this experiment, ten scans were repeated over the same line path. The red vertical lines indicate the time at the beginning of each successive laser scan for this line path. From this figure, it is apparent that no measurable current is observed at any point during the scanning process.

Figure 2.2b shows the current measured versus the laser scanning time for a line path scanned under the same nominal conditions as that shown in Fig. 2.2a (scan speed of 100 mm/s, laser power of 20 W, with ten scan repetitions over the same line path), except that an electric field of 3000 V/cm was applied during laser scanning. Again, there is no measurable current observed for the first two repeated scans of the laser. During the third scan, however, the current rises to about 2 μA near the end of the scan. For subsequent scans over the same line path, the current then rises with an overall trend that is monotonic for the fourth and all successive scans, reaching a peak of approximately 60 μA at the end of the 10^{th} and final laser scan. Note that there are small variations from the overall trend in the peak currents from scan to scan because the data acquisition speed was not fast enough to capture the true peak in current.

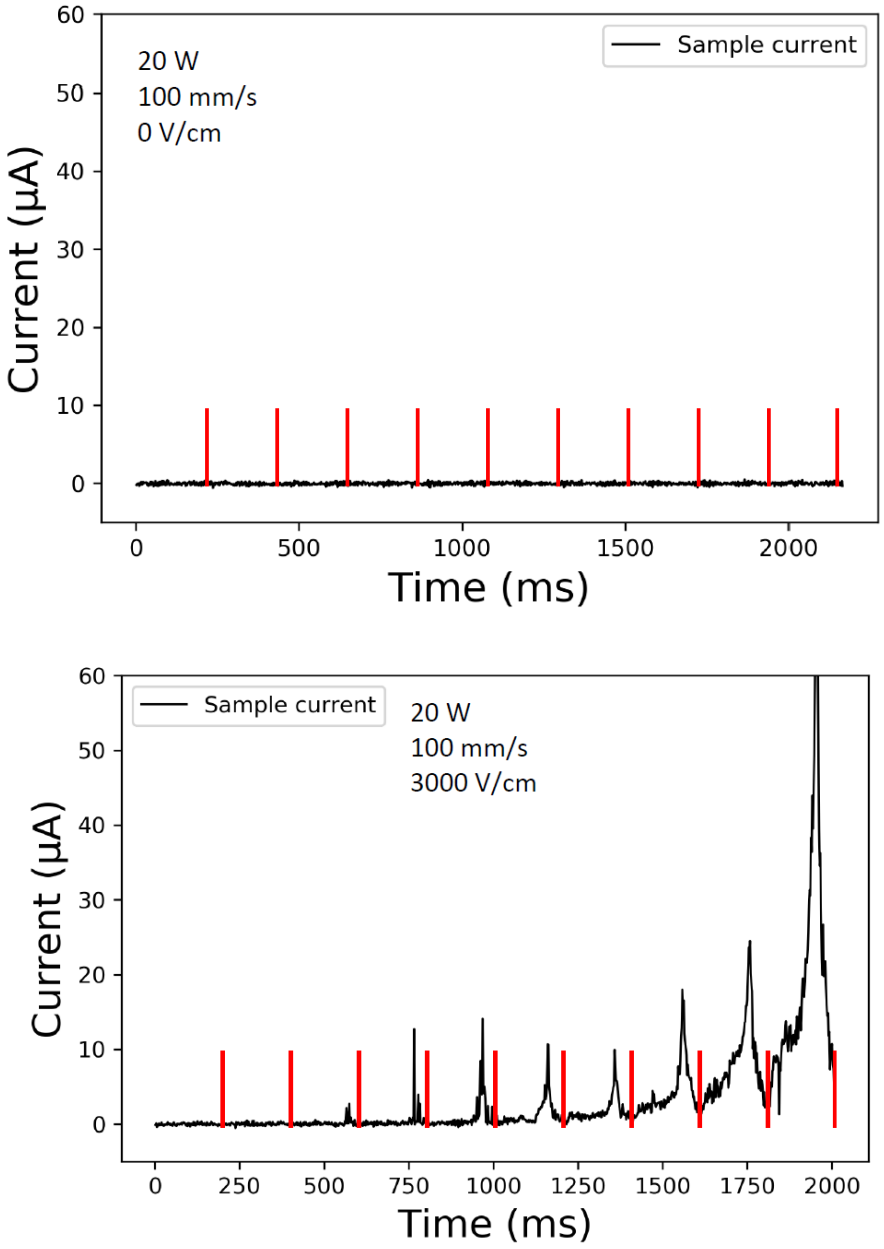

Figure 2.2. Current measured (black line) from 10 repeated scans of the same line path at a laser power of 20 W and a laser scan speed of 100 m/s: a) No applied electric field and b) With an applied electric field of 3000 V/cm. Vertical red lines indicate approximate time when each laser scan completed.

The microstructures of the samples before and after laser scanning are shown in Fig. 2.3. In Fig. 2.3a, the microstructure on the surface of a representative green pellet is shown. The powder particles range in size from approximately 0.5 – 5 μm and are irregularly shaped with sharp features. Figure 2.3b shows the surface of a region of pellet that was scanned 10 times with a laser scan speed of 100 mm/s, laser power of 20 W, and an electric field of 0 V/cm. The particles do not appear to be significantly changed relative to those shown in Fig. 3a, indicating that the repeated scanning under these scan conditions without an applied electric field did not alter the microstructure. Figure 2.3c shows the surface of a region of pellet scanned 10 times with a laser scan speed of 100 mm/s, laser power of 20 W, with an electric field of 3000 V/cm present. Compared to the microstructures shown in Figs. 2.3a or 2.3b, the microstructure shown in Fig. 2.3c is significantly different. There are visible necks formed between many of the particles and many of the sharper features that were present in the green pellet are rounded after SLFS.

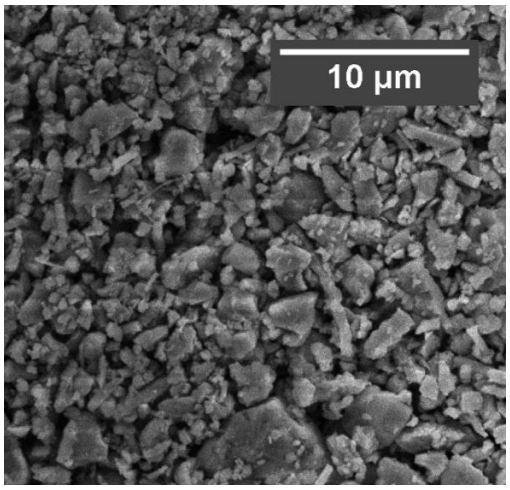
10 µm

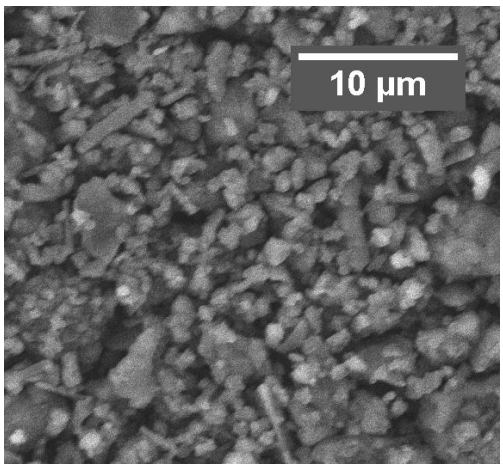
10 µm

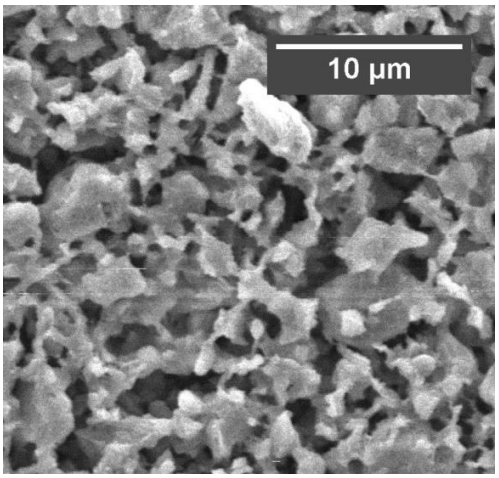

Figure 2.3: SEM micrographs of a) green pellet, b) pellet after laser scanning 10 times with no applied field at a scan speed of 100 mm/s and laser power of 20 W and c) pellet after laser scanning 10 times with applied field of 3000 V/cm at a scan speed of 100 mm/s and laser power of 20 W.

Figure 2.4 shows the measured current from three different line paths that were scanned with differing laser powers. All of these line paths were scanned with an electric field of 3000 V/cm, a laser scan speed of 100 mm/s, and with 20 scan repetitions of the laser over the same line path. The figure shows that for a laser power = 10 W, no observable current is visible until the fifteenth scan repetition, when current rises slowly and monotonically up to about 30 µA for the last repetition. At a laser power = 20 W, no measurable current is obtained until about the fourteenth repetition, when it rises to about 40 µA. During the subsequent scan, the current increases dramatically and exceeds the current limiter on the power supply (i.e. current runaway). At a laser power = 30 W, measurable current is first obtained during the third repetition and increases for the fourth repetition before run-away is observed during the fifth repetition. For subsequent scan repetitions, the current drops to 25 µA and remains approximately constant for several

scans before slowly dropping towards zero. The trend for these three experiments shows a strong correlation between laser power and observed onset of SLFS, with greater laser powers both causing higher observed current and current runaway at earlier times.

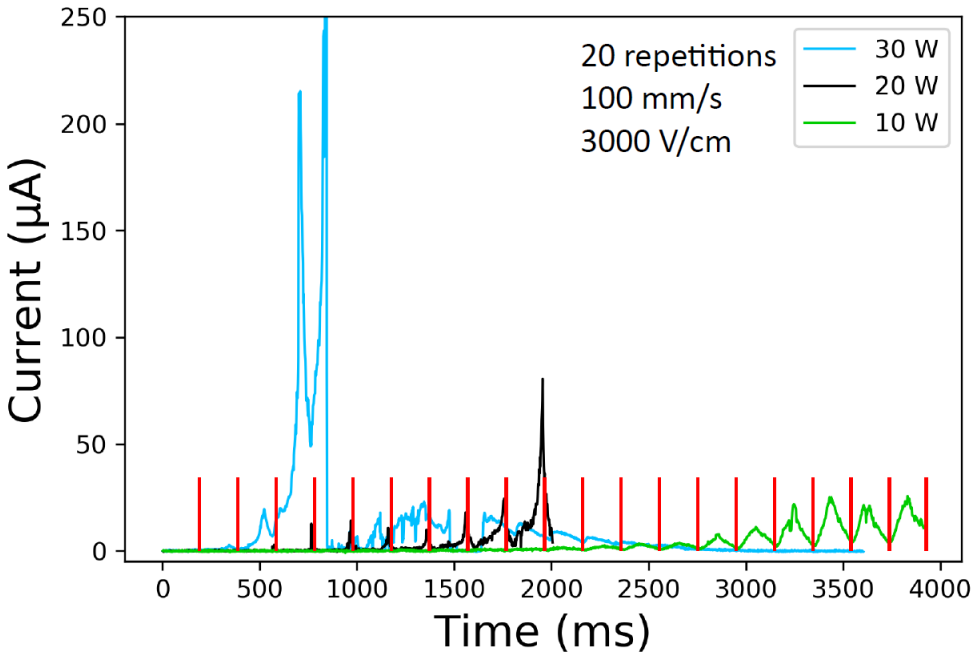

Figure 2.4: Current measured through samples at laser powers of 10, 20 and 30 W. Vertical red lines indicate approximate time when each laser scan completed.

The relationships between observed current through the sample and the laser scan speed is explored further in Fig. 2.5. For these experiments the laser power was fixed at 20 W, the applied electric field was fixed at 3000 V/cm, and each line path was scanned for 20 repetitions. At a scan speed = 200 mm/s, there is minimal observed current until the last few repetitions when it increases to about 2 μA before the 20th and final repetition. When the scan speed is reduced to 100 mm/s, there is initially no observed current. After 1600

ms (the 8th repetition), the current begins to rise slowly for each subsequent scan repetition until it reaches approximately 10 µA at around 3000 ms. The last four laser scan repetitions show a large spike in observed current, where current rises to a maximum of around 25 µA before the 20th and final repetition. When the laser scan speed is reduced further to 33 mm/s, there is again no measurable current for approximately 1600 ms before the current begins to increase. Note however, that this corresponds to 4th scan repetition at this slower scan speed. As was observed for the scan speed of 100 m/sec, the current continues to rise monotonically until plateauing near 50 µA. There is considerably more variation in current from one scan repetition to the next at the slower scan speeds compared to that observed at faster scan speeds.

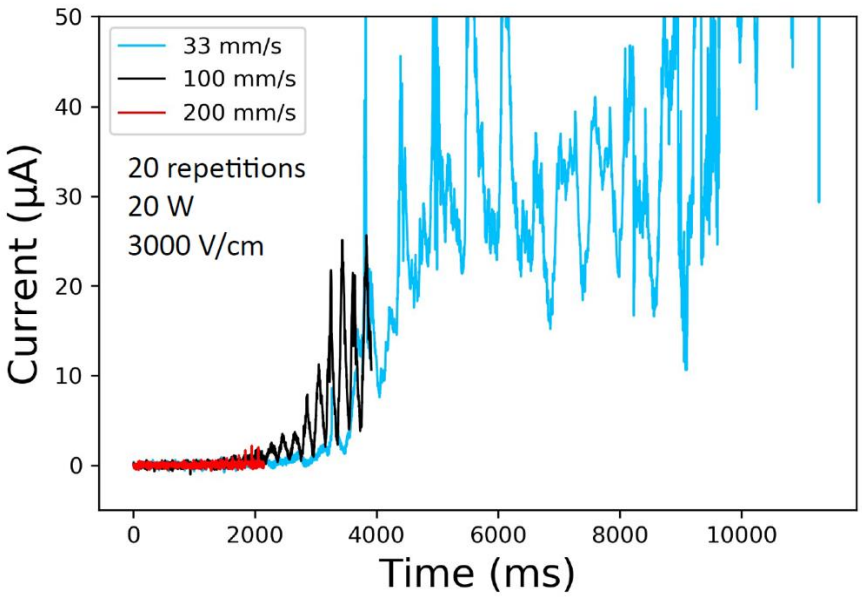

Figure 2.5: Current measured through samples at laser scan speeds of 33, 100, and 300 m/s.

The data in Figs. 2.4 and 2.5 show that the onset of SLFS can be triggered with fewer scans by decreasing the laser scan speed or by increasing the laser power. This suggests that the relevant parameter that governs the onset of SLFS may be related to the heat input, β, which is the product of the laser power intensity and the laser interaction time. To test this hypothesis, Fig. 2.6 shows the current measured while varying the laser power intensity and laser scan speed. Figures 2.6a and 2.6b compare the current versus time for a constant $\beta = 6 \times 10^{-5}$ J/mm^2. At slow scan speeds and low laser powers (Fig. 2.6a) only very small currents are measured that are close to the resolution limits of the instrument. In contrast, when the scan speed and laser power are increased while maintaining a constant β (Fig. 6b), the current begins to increase after the 4th repetition and continues to increase monotonically with successive repetitions. Figures 2.6c and 2.6d compare the current versus time for a constant $\beta = 3 \times 10^{-5}$ J/mm^2. At the lower scan speed and current (Fig. 2.6c) there is again no observed current. Increasing the current and laser power simultaneously (Fig. 2.6d) again results in an increase in current after multiple laser scan repetitions.

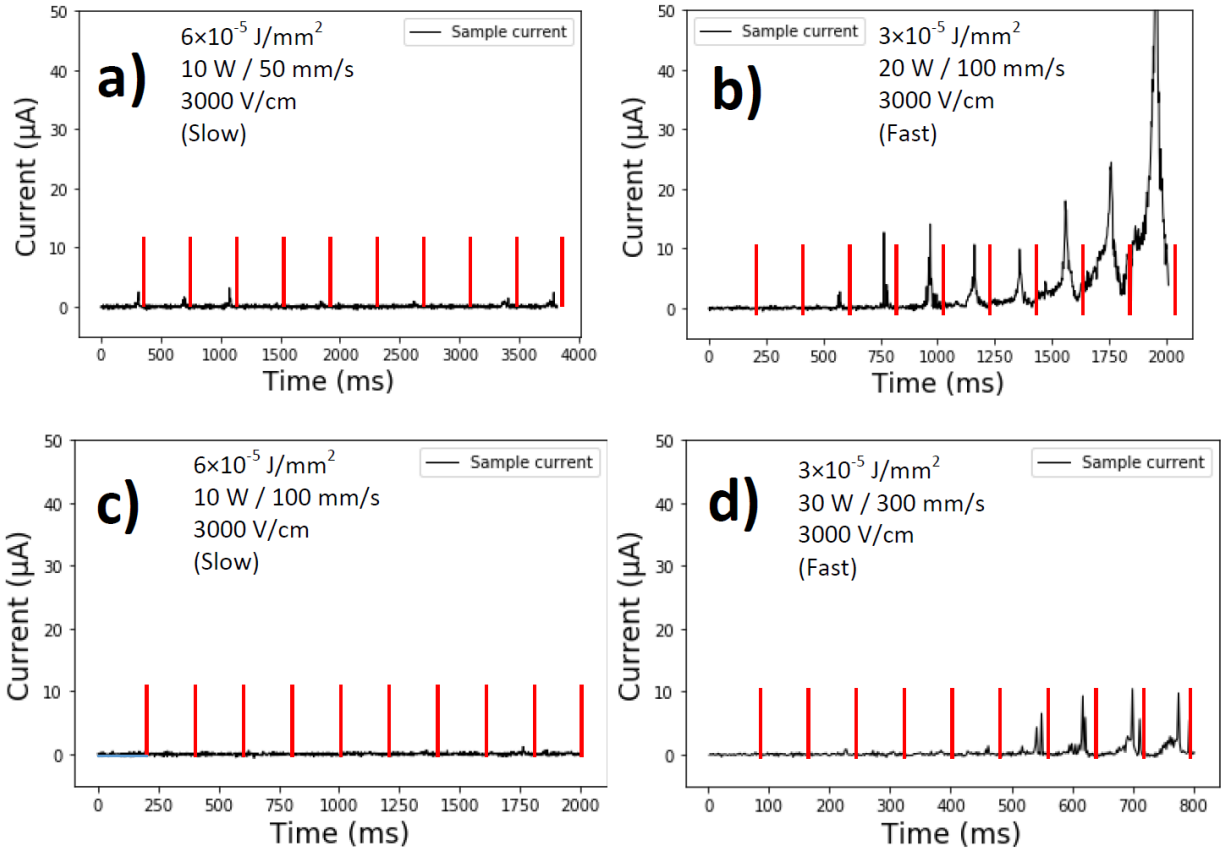

Figure 2.6: Current observed through samples versus time for a) and b) $\beta = 6 \times 10^{-5}$ J/mm^2 and c) and d) $\beta = 3 \times 10^{-5}$ J/mm^2. Vertical red lines indicate approximate time when each laser scan completed.

Figure 2.6 shows that onset of SLFS of AlN cannot be related directly to β because the conditions required to initiate SLFS were found to vary even when β was fixed. SLFS was found to initiate most readily at high laser powers, slower scan speeds and large β. Together, these results suggest that heat input is only one important variable that influences the initiation of SLFS. These results also suggest that heat dissipation must also plays an important role in SLFS.

2.4 Numerical Model of Heat Flow during SLFS

To explore the effects of both heat input and heat dissipation on the temperature of the scanned region during SLFS, a numerical model was developed using COMSOL Multiphysics® software (Comsol Inc., Burlington, MA) to study the dynamic heat distribution in the pellet during the SLFS process. Minimum temperatures were studied within the region across which the laser scans, this region is illustrated schematically in Fig. 2.7. This line region is defined as a hemicylinder with a diameter equal to the beam diameter of 400 μm and a length equal to the scan path length.

For the numerical model, the AlN powder bed was modeled as a continuous domain with effective materials properties. The only heat source that was considered was the laser and it was assumed that heat dissipation occurred due to a combination of conductivity through the solid, radiation from the surface of the pellet, and convection from the pellet to the surrounding N_2 gas. The thermal conductivity for the AlN powder bed was calculated from a powder bed model (41) which yielded values from 0.5 W/(m·K) at room temperature up to 1 W/(m·K) at 2000 K. The density of the powder bed was taken as 1.4 g/cm^3 and the specific heat was assumed to be 780 J/(kg·K). Because the laser absorption depth is difficult to determine for a powder bed, a simplified heat source model was used. The laser was assumed to be a 3D Gaussian heat source, with a 1/e radius of 279 μm and a heat penetration depth of 100 μm. The effective reflectivity from the powder bed surface was assumed to be 20% (i.e. a total of 80% of the laser power was absorbed to a depth of 100 μm). The sample interaction domain with the laser was modelled as a 2 mm x 1 mm x

11 mm region, encapsulating the full length of a laser scan across the pellet surface. Further details of how the simulations was conducted are provided in the appendix.

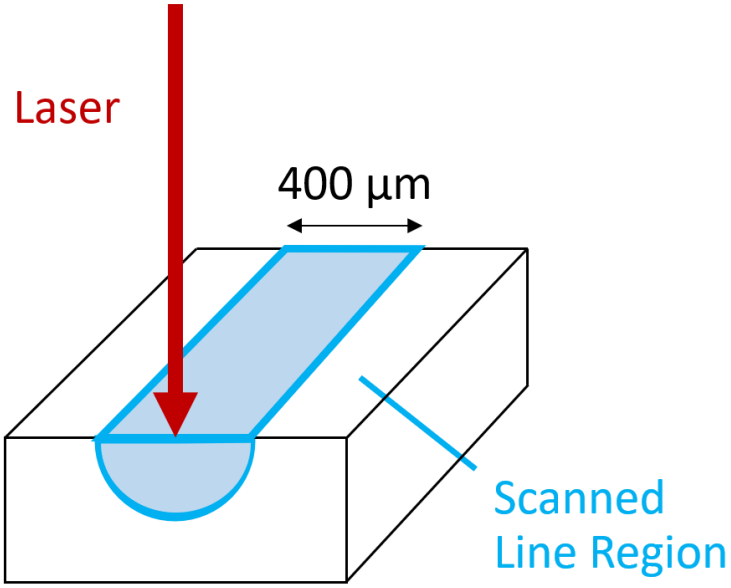

Figure 2.7: A schematic showing the scanning laser and the line region where the minimum temperature was computed (blue).

Figure 2.8 shows experimental data and predictions from a simulation performed assuming the same scan conditions used in the experiment. The scan distance traveled and the scan times are both slightly longer for the experiment compared to the simulation because in the experiment, the scan started and completed on the electrode; the extra distance traveled by the laser and the delays between succeeding scan lines were not accounted for in the simulation. To facilitate comparisons between the times in the experiment and simulations, the scan times were normalized by the total scan time for the experiment (τ = normalized scan time). Figure 2.8a is a plot from an experiment of

measured current for a line path scanned under an electric field of 3,000 V/cm, a laser power of 20 W, a laser scan speed of 100 mm/s, and with 10 scan repetitions of the laser over the same line path. During the 4th scan, a small rise in current is visible. **Figure 8b** shows the predicted minimum temperatures obtained from the numerical model for the same conditions shown in Fig. 8a. The overall trend is that the temperature rises during each scan and from one scan to the next. The time the laser is off is determined by the jump speed which is 1m/s in all cases, and the time the laser is on is determined by the laser scan speed (variable for these simulations) and the length of the line, which is 1.1 cm. From the experiment shown in Fig. 2.8a that SLFS initiates during the 4th line scan, the corresponding predicted minimum temperature from the simulation during the 4th line scan is T=475 K.

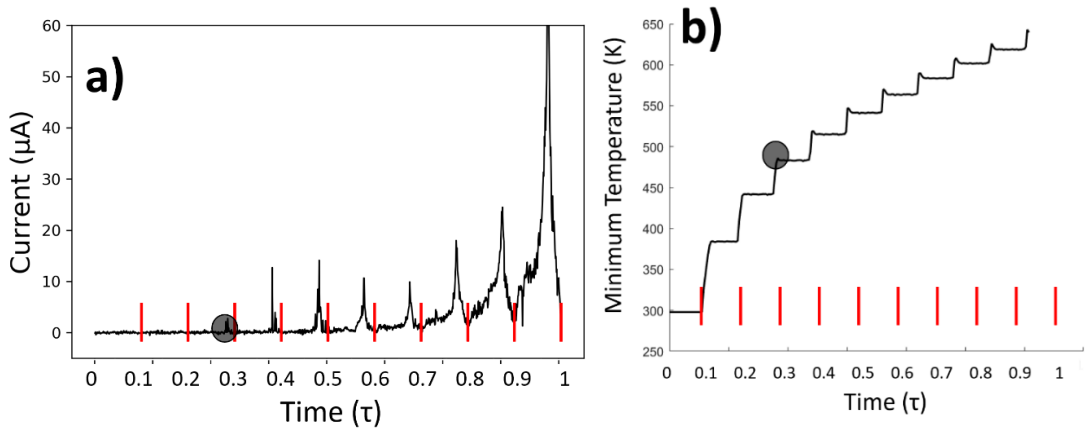

Figure 2.8: a) Experimental results showing the current versus normalized time b) Predictions from the numerical model showing the average temperature of the scanned line region versus normalized time during repeated scans of the same line path. The dots in both a) and b) indicate the onset of SLFS and the vertical red lines indicate the approximate times when the laser scans completed.

Figure 2.9 shows the predicted minimum temperatures in the scanned line region obtained from the numerical model for four different experimental conditions: i. laser power = 10 W, scan speed = 50 m/s, ii. laser power = 10 W, scan speed = 100 m/s, iii. laser power = 20 W, scan speed = 100 m/s, and laser power = 30 W, scan speed = 300 m/s. For the two cases where the laser power is 10 W, the predicted temperatures both increase quickly and reach approximately 450 K in about $\tau = 0.4$ ($t \approx 1$ s) before the rate of temperature increase slows as the influence of heat dissipation becomes more significant at longer time scales. The minimum temperature consistently occurs directly ahead of the beam because this region has had the most time to cool since the last laser scan. As most of the cooling occurs immediately after the laser passes, scan speed differences have a decreasing effect on minimum temperature when slower scan speeds are employed and the cooling time between passes increases. The two scan speeds for the 10 W case are thus sufficiently slow that the minimum temperatures are similar. When the laser power is increased to 20 W, the minimum temperature within the line rises to 475 K by the time $\tau = 0.2$. The temperature in the line path scanned at 30 W rises even more quickly reaching the same temperature by $\tau = 0.1$.

The required number of repeated scans along the same line path to initiate SLFS was measured experimentally and the corresponding number of repeated scans from the simulations is indicated in Fig. 2.9 with dots. By plotting the data in this way, the predicted minimum temperatures to initiate SLFS can be obtained from the simulations for each scan condition. This plot shows that the highest predicted temperature for the onset of SLFS of about 480 K occurs at $\tau = 0.2$ ($t \approx 0.15$) s when the laser is scanned at 20 W. Reducing the

laser power reduces the onset temperature for flash and increases the time required to initiate SLFS. For a laser power of 10 W, the onset of SLFS occurs at a temperature of 450 – 475 K and requires $\tau = 0.4 – 0.5$ ($t \approx 1.0 – 1.25$ s).

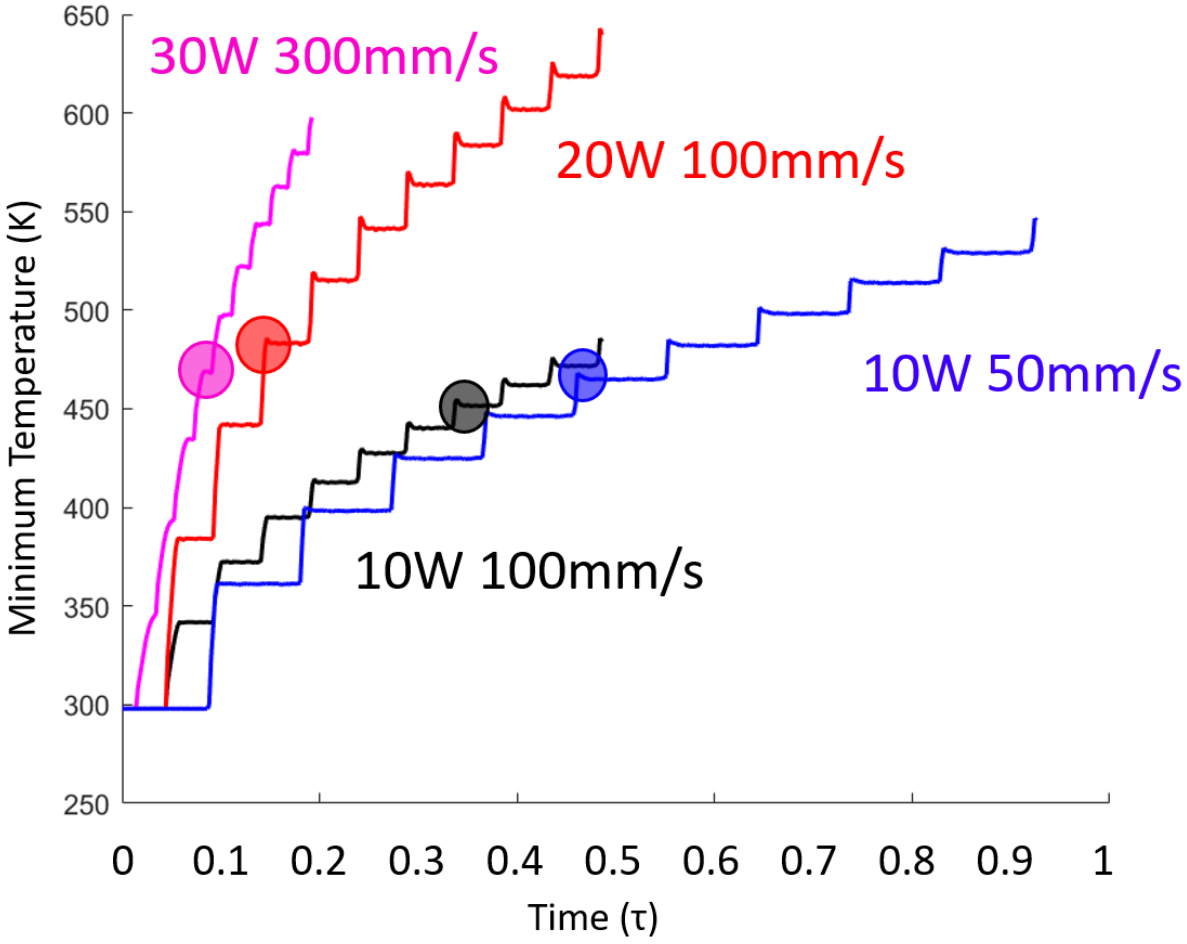

Figure 2.9: The predicted minimum temperatures from the numerical simulations within the scanned line region. Dots represent the predicted temperature/times for the onset for SLFS. Each dot represents the average initiation time from four experiments.

2.5 Discussion

This paper presents the first direct microstructural evidence of SLFS by correlating measured currents from experiments to neck formation between powder particles. This is evident from Figure 2.3c, where particle necks have clearly formed following a laser scan under an electric field of 3000 V/cm. When no electric field and current was applied, necks do not form (Figure 2.3b), nor is current detected through the sample. From this observation it is clear that when sufficiently large electric fields and laser powers are applied, neck growth accompanies measured current and both observations are indicators of the onset of SLFS.

This paper also presents the first experimental evidence that flash sintering can occur in nitrides. Because both nitride and carbide powders may exhibit surface oxidization, and because conduction occurs primarily in the near surface regions, the presence of oxides is likely to influence the onset conditions for SLFS. TEM was performed of the powders to determine if the surfaces were oxidized. These images (not shown) confirmed that the AlN powder contained a thin (<5 nm) of oxide on the surface. The presence of a thin surface oxide on AlN is difficult to prevent and cannot be easily eliminated once it occurs. Thus, from a practical perspective the oxide must be treated as part of the specimen and it remains an open question as to whether nitrides such as AlN are intrinsically able to be flash sintered in the absence of a surface oxide.

Experiments shown in Figs. 2.4 and indicate that heat input is one parameter that determines the onset of SLFS. The heat input depends on both laser power and scan speed and both parameters can be varied to control heat input. Figure 4 shows that for a fixed

scan speed, increases in laser power result in a reduction in the time necessary for the onset of flash sintering and larger currents flowing through the sample once SLFS initiates. Figure 2.5 shows that, at a fixed laser power, slower scan speeds reduce the number of repeated scans required to initiate SLFS and increase currents flowing through the sample once SLFS initiates.

To test the hypothesis that heat input solely determines the onset of SLFS, experiments were conducted under conditions of constant heat input (β = laser power × scan speed). Figure 2.6 showed that while β does influence onset conditions; it is not the sole parameter that determines the onset of SLFS. This is unlike YSZ, which has a much lower thermal conductivity and flashes after a single scan, indicating that the conditions for the onset of SLFS for YSZ are primarily governed by the heat input. (5) Subsequently, it was hypothesized that the onset of flash sintering at a given electric field occurs when the minimum temperature in the scanned line reaches a critical temperature. The temperature within the line depends on both heat input and heat dissipation and thus both play a significant role in SLFS of AlN.

A numerical model was developed that accounted for both heat input and dissipation during repeated scanning of a line path across the sample from one electrode to the other. The model showed that a minimum temperature of 450 – 500 K must be reached everywhere along the scanned line region in order for SLFS to initiate. Previous studies of furnace-based flash sintering have shown a minimum temperature is required for flash to initiate (36,37). For SLFS we postulate that the minimum temperature to initiate flash is related to the minimum conductivity along the laser scan path. Thus, the lowest temperature

controls the effective conductivity of the entire scan path. Once this effective conductivity has increased beyond a certain threshold at a specific electric field, current begins to flow and the flash initiates.

SEM observations of the samples after laser scanning revealed that many of the samples exhibited channel cracks that were oriented perpendicular to the scanning directions in the regions that had been scanned multiple times. This explains the non-monotonic behavior observed in some samples that is most clearly evident in Fig. 2.4 for the scan condition with a laser power of 30 W. For this scanning condition, the measured current first rises quickly for the first four successive scans before dropping for subsequent scans. These results suggest that repeated scans at combinations of high laser powers and low scan speeds leads to thermal shock cracking that reduces the subsequent current flow through the sample. This is also notable because the onset of cracking would be expected to significantly alter heat flow only if it occurred *before* the onset of SLFS. For most of the scan conditions studied here, the monotonic rise in the current for at least several repeated scans following the initiation of SLFS suggests that cracking occurred during subsequent repeated scans or during cooling after the last scan. However, further work is needed to confirm this.

It is important to note that cracks are not intrinsic to the SLFS process. Although we observed cracking for some experiments during repeated scanning conducted over an exceedingly broad range of scanning conditions, it should be possible to scan under narrower range of conditions that do not produce cracks by limiting the scan speed and laser power. It may also be possible to scan under a broader range of conditions without

cracking by actively controlling the field during scanning and we are currently exploring this possibility.

2.6 Conclusions

Experiments showed that SLFS can be observed in AlN and this was confirmed from both current measurements through the sample and observed microstructural changes following selective heating using a scanning laser under an applied electric field. Compared to materials with lower thermal conductivity such as YSZ, the conditions for initiating SLFS in AlN require combinations of higher laser, slower scan speeds, or repeated scans of the same region of the sample surface. It was shown that laser power and scan speed both have effects on the current observed during SLFS, but neither is a direct controlling factor for the onset of SLFS. The heat input, β, calculated from the product of the power intensity and the laser interaction time was also studied as a possible controlling factor. These experiments showed that β also does not directly control the onset of SLFS and that both the heat input and heat dissipation affect the onset conditions for SLFS.

A numerical model was implemented that accounted for heat input and heat dissipation and it was shown that, for a given field strength, the initiation of SLFS in AlN is controlled by the minimum temperature in the scanned line region and the time that this region remains at or above this temperature. The temperature in this region is in in turn controlled by laser scan speed, laser power, and the effective thermal conductivity of the sample. For SLFS conducted on AlN under an applied electric field of 3000 V/cm, the time

to initiate SLFS is reduced from 1.0 – 1.25 sec when the minimum temperature in the line scan region reached 450 – 475 K to approximately 0.25 s when the minimum temperature in the line regions reached 480 K. Similar dependences between time to initiate flash and sintering temperature have been observed during furnace-based flash sintering at lower fields in oxides and work is ongoing to understand the atomic-scale phenomena responsible for this behavior in both furnace-based flash sintering and in SLFS.

2.7 Appendix

A numerical model was developed and implemented in Comsol® to predict the onset conditions for SLFS for aluminum nitride. Input for this model required knowledge of the material properties of the AlN powder bed. Rather than performing simulations at the scale of individual powder particles, an effective medium approach was used. In the sections that follow, the methodologies used to obtain these properties are outlined and the details of the model implementation are outlined.

Material Properties

The bulk thermal conductivity of 320 W/m·K (38) and the gas conductivity for N2 at room temperature of 0.027 W/m·K (39) were obtained from the literature. A number of approaches were used to obtain effective properties that depended on the specific properties of interest. For some properties such as the coefficient of specific heat and the density, a simple rule-of-mixtures can be used to predict effective properties of a porous medium. Thus, the coefficient of specific heat (780 J/kg·K) (40) and an effective density (1,470 Kg/m^3) was computed from the product of the bulk properties of AlN and the measured porosity of the green parts (=45%).

The effective thermal conductivity cannot be obtained from a simple rule-of-mixtures. Instead, a model by Sih & Barlow (41) was used and validated with thermal

conductivities of packed powders obtained from the literature (42). The effective thermal conductivity was obtained from Equation A-1:

$$\frac{k}{k_g} = (1-\sqrt{1-\varphi})(1+\frac{\varphi k_R}{k_g}+\sqrt{1-\varphi}\left\{(1-x)\left[\frac{2}{1-\frac{Bk_g}{k_s}}\left(\frac{B}{\left(1-\frac{Bk_g}{k_s}\right)^2}\left(1-\frac{k_g}{k_s}\right)\ln\frac{k_s}{Bk_g}-\frac{B+1}{2}-\frac{B-1}{1-\frac{Bk_g}{k_s}}\right)+\frac{k_R}{k_g}\right]+x\frac{k_{contact}}{k_g}\right\} \quad \text{(Eq. A1)}$$

where φ = the porosity of the powder compact, x = contact size ratio = area of particle in contact with neighboring particle/total area of the particle, k_g = the gas thermal conductivity, k_s = the bulk thermal conductivity, $B \approx 1.25\left(\frac{1-\varphi}{\varphi}\right)^{\frac{10}{9}}$, $k_{contact}$ = the contact thermal conductivity = $18\varphi k_s$, k_r = radiative thermal conductivity, and k = effective thermal conductivity of the powder bed. Table I shows that there is reasonable agreement between the effective thermal conductivity predicted from the model and the experimental values obtained from measurements.

	k_s W/m·K	k_g W/m·K	φ	Experimental k W/m·K	Calculated k W/m·K	% difference
Steel spheres in air	38.4	0.026	0.38	0.525	0.486	7.3
Steel spheres in air	45	0.0272	0.413	0.40	0.45	-13
Steel spheres in air	45	0.0272	0.406	0.60	0.46	22
Lead spheres in air	34.3	0.0273	0.42	0.418	0.420	-0.69
Lead spheres in air	34.3	0.0273	0.433	0.404	0.399	1.16
MgO in air at 375 K	24.4	0.0318	0.42	0.433	0.446	-3.0
MgO in air at 502 K	27.9	0.0387	0.42	0.502	0.536	-6.8
MgO in air at 572 K	22.1	0.045	0.42	0.552	0.575	-4.2
MgO in air at 723 K	16	0.0533	0.42	0.661	0.609	7.7

MgO in air at 810 K	13	0.056	42	0.666	0.601	9.7
					Average % difference	1.9

Table 2.1 Validation of empirical Zehner model for thermal conductivity of various packed powder beds

A parametric study was performed to determine the effects of porosity, contact size ratio, and bulk thermal conductivity on the predicted thermal conductivity and results are presented in **Figure A-1a-c.** For these calculations, one variable was varied while holding the other variables fixed at standard values that were in the range of interest for SLFS experiments. The standard values that were used were x=0, φ=.43, and k_s=320 W/m·K.

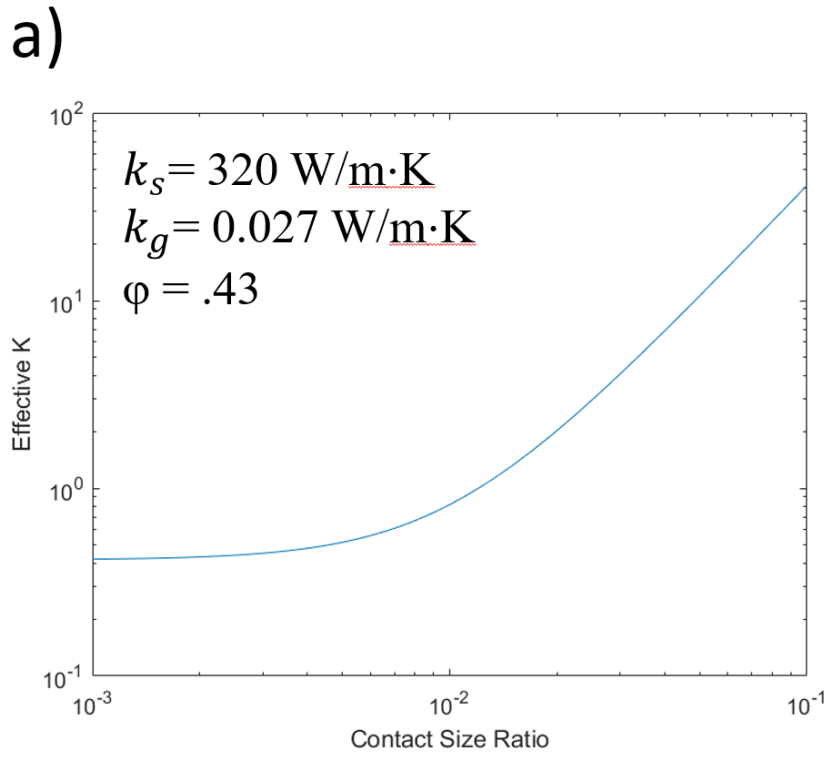

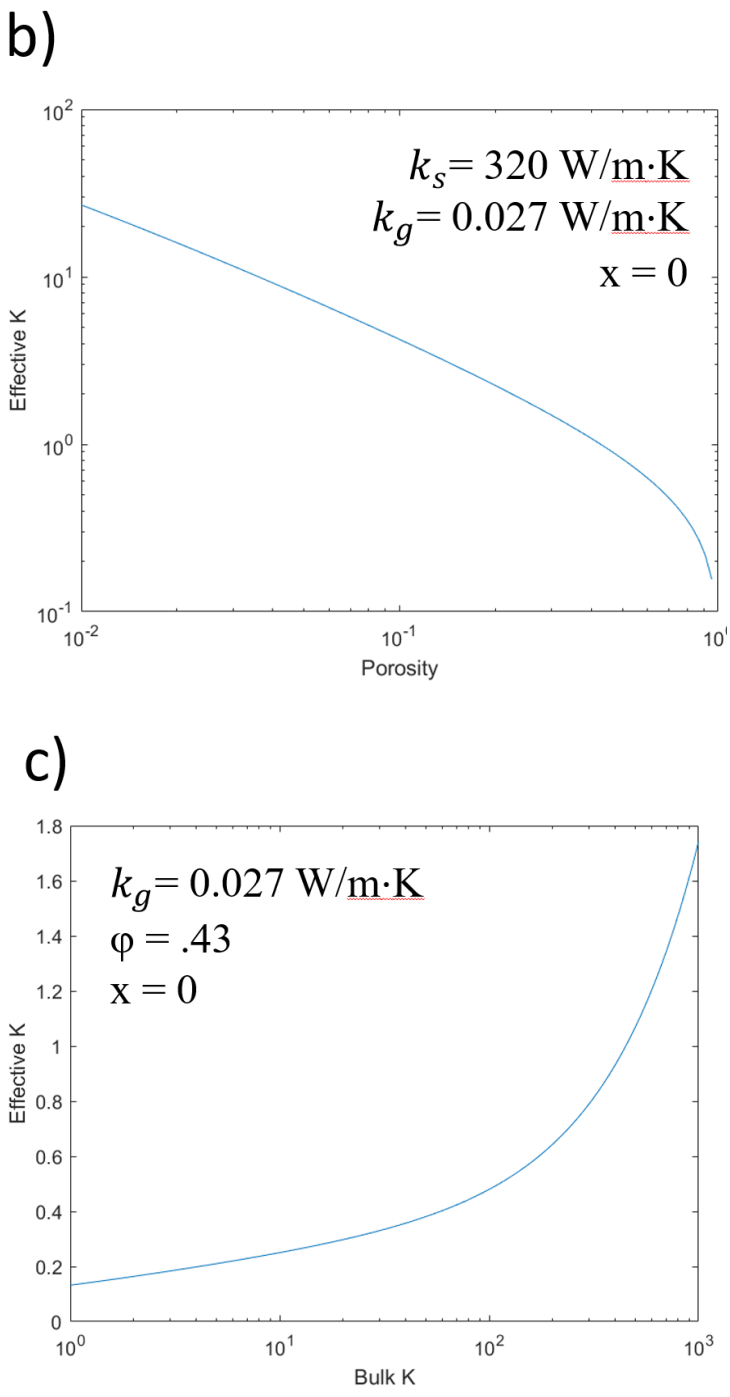

Figure 2.10: Effective thermal conductivity, K, versus a) contact size ratio (x), b) porosity (φ), and c) bulk thermal conductivity (k_s).

It can be seen from Figure 2.10 (a) that the effective thermal conductivity remains fairly constant for contact size ratios 0 to 0.01, and then increases logarithmically as the contact size ratio increases. This shows that $k_{contact}$ is negligible when the particle neck sizes are small near the onset of SLFS and thus for the remaining calculations it was assumed that $k_{contact} = 0$. From Fig 2.10 (b), it is seen that the effective thermal conductivity initially decreases logarithmically with porosity until a porosity value of 0.1, and then decreases even more rapidly as porosity approaches 1. Fig 2.10 (c) shows that the influence of the bulk thermal conductivity on the effective thermal conductivity is modest for the values of x and φ that were used. Because this plot showed that the bulk thermal conductivity did not significantly influence the effective conductivity, a constant value of k_s = 320 W/m·K was used in the numerical model and the temperature-dependence of the effective conductivity was assumed to arise entirely due to the changes in gas thermal conductivity, as given by Eq. A-1. The thermal conductivity of nitrogen varies from 0.027 W/m·K at room temperature to a maximum of 0.110 W/m·K at 2000 K**.** (39) This resulted in an effective thermal conductivity for the porous aluminum nitride compact of between 0.52 and 1.1 W/m·K, depending on temperature.

Heat Source

A 3D Gaussian heat source model given in equation A-2 was used to represent the laser heat source: ([43])

$$q = \frac{2\varepsilon P}{\pi R^2 S} \exp\left(-\frac{2\left((x-Vt)^2+y^2\right)}{R^2}\right) \exp\left(\frac{-|z|}{S}\right) \qquad \textit{Eq. A-2}$$

where P = the laser power, R = the beam radius, V = the laser scan speed, S = the beam penetration depth, x, y, and z are the coordinates being probed, t = time, and ε is the percent energy of the laser absorbed by the material surface. The heat source model used a beam radius of 200 μm and a penetration depth of 100 μm, as determined from beam profiling and SEM observation of samples, respectively (NanoScan v2™, Ophir, Jerusalem, Israel). The numerical model was validated by comparing temperature distributions in the numerical model with those from an analytical model for the temperature distribution for a moving gaussian beam derived by Sanders (1984) (44).

CHAPTER 3: NUMERICAL SIMULATION OF JOULE HEATING OF ALUMINUM NITRIDE NANOPARTICLES

3.1 Introduction

Previous simulation work on the processes of ceramic sintering have been primarily focused around continuum-based numerical modeling of ceramic media (45,46,47). In modeling of flash sintering, research has focused on either analytical (9,48) or continuum-based modeling of the sintering process (49). To better understand the physics of selective laser flash sintering, it is imperative that an understanding be obtained of how the micro-scale sintering process changes in response to various operating conditions. In this work, a parametric study is conducted whereby simulated aluminum nitride nanoparticles are subject to various combinations of volumetric power densities, electric fields, and contact size ratios.

3.2 Numerical Model

A numerical model was created using COMSOL Multiphysics® software (Comsol, Burlington, MA) to simulate the heating of aluminum nitride particles subjected to various electric fields and applied volumetric power densities that are meant to simulate laser heating. It emphasized that these power densities are volumetric and are not the same as the commonly used laser power densities, which are two dimensional. The model consisted of three particles of aluminum nitride, each with a diameter of 1 μm. The contact size ratio refers to the proportion of area of a particle in contact with another particle, divided by the total surface area of the particle. The structure of the particles in the model as well as the placement of electric potential is shown in Figure 3.1.

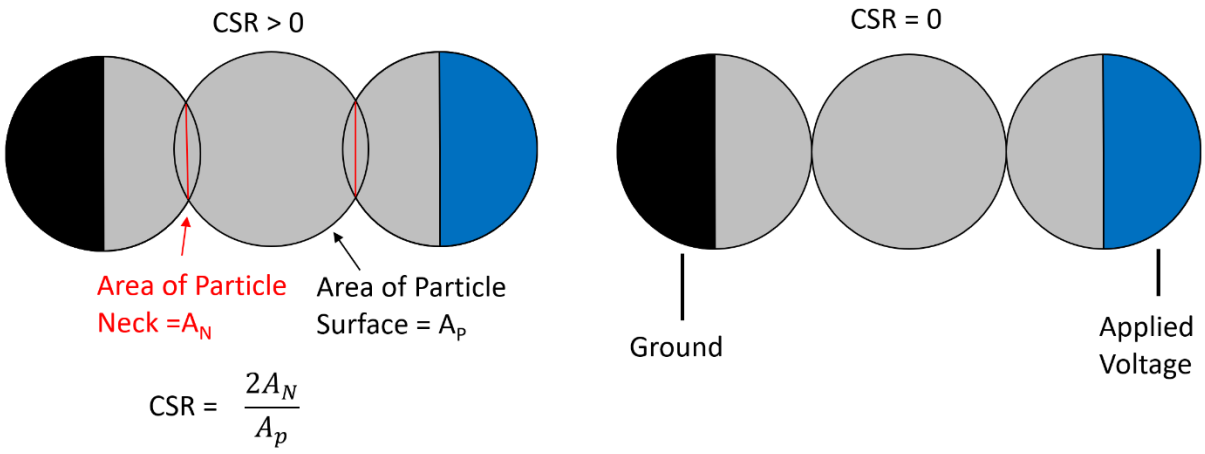

Figure 3.1: The structures of the particles simulated with a contact-size ratio greater than zero (left) versus one with a contact size ratio of 0 (right), as well as the location of applied voltage and ground

The particles were first uniformly heated by a volumetric heat source to approximate the laser heating process. The properties for the particles were assumed to be those of bulk aluminum nitride, with a thermal conductivity of 320 W/m·K, a specific heat of 780 J/kg·K, and a density of 3,260 kg/m^3 (37). The electrical conductivity was assumed to be an exponential function varying with temperature, starting at effectively zero at room temperature and rising beyond 1×10^{-5} S/m at approximately 900 K (50). The electrical conductivity is important because it controls the amount of additional heating that arises from Joule heating.

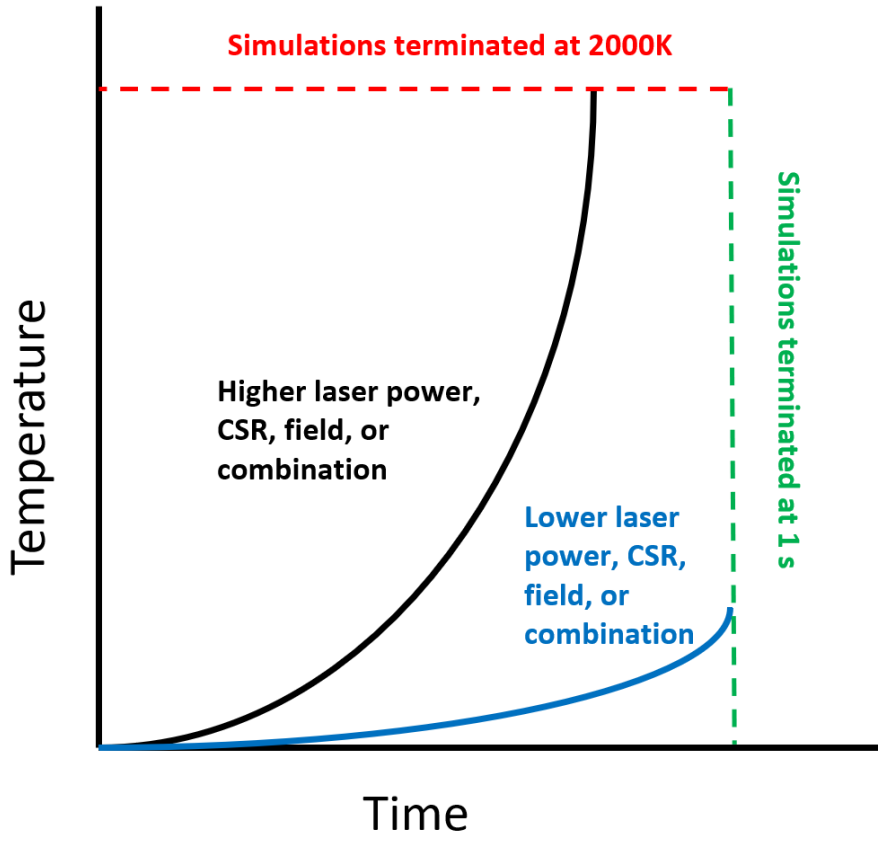

Figure 3.2: Termination conditions for various temperature vs time curves from parametric analysis, showing two end conditions (one temperature and one time based) as well as two possible temperature vs time curves with different controlling parameter values

Figure 3.2 shows a representative output of two simulations run with two different sets of parameters. The key parameter being tracked is the temperature of the particles as a function of time, with the goal of determining how long it takes for the temperature to rise due to combined external volumetric heating and Joule heating. The curves for all cases increase exponentially; although temperature initially rises linearly, the temperature-dependent electrical conductivity causes an even sharper rise as Joule heating commences.

Higher field strengths, higher laser powers or in this case volumetric power densities, and larger contact size ratios are expected to cause steeper increases in temperature than lower fields, lower power densities, or lower contact size ratios. Due to the limitations of the numerical model, simulations were either ended when a temperature of 2000 K was reached, or when one second had elapsed, whichever came first.

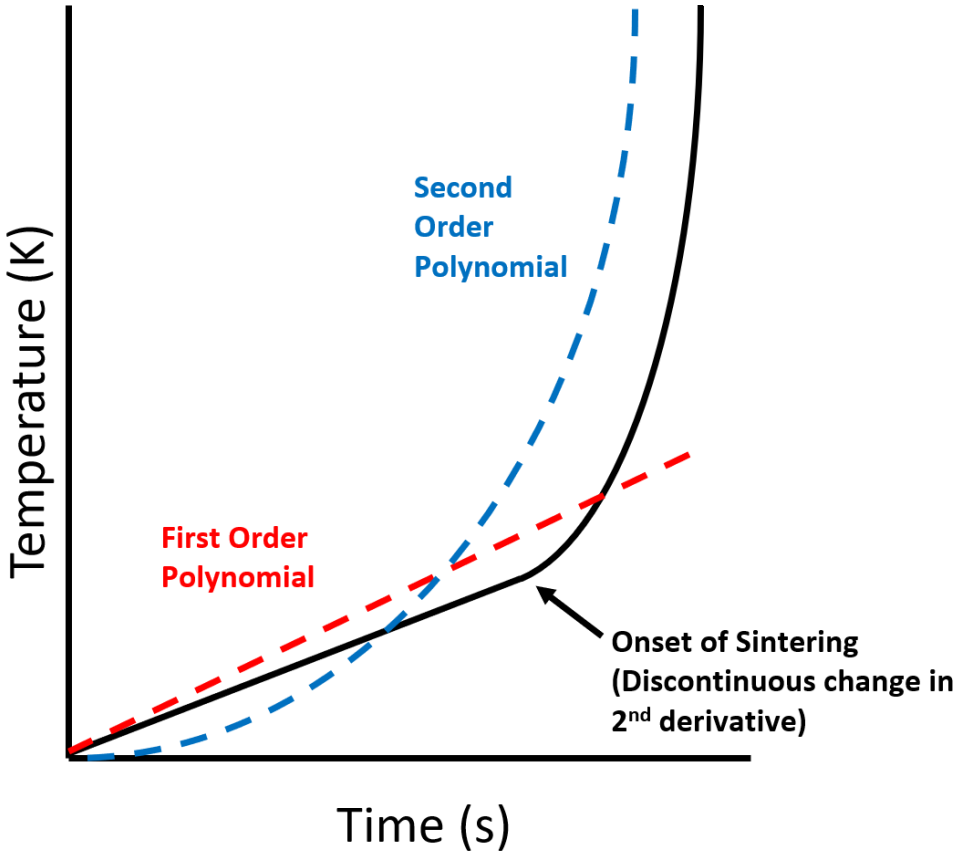

Figure 3.3: The two different polynomials fitted to various temperature vs time curves. The first order polynomial captures the initial temperature rise while the second order polynomial captures the initiation of sintering

Due to the varying termination conditions, the results for various parametric combinations could not be directly compared with respect to either of those two metrics. Data was instead compared by generating 1^{st} and 2^{nd} order polynomials fit to the temperature curves, and then the 1^{st} and 2^{nd} derivatives of each polynomial were analyzed, respectively. The polynomial curves and how they are influenced by the temperature vs time curve is shown in Figure 3.3. From this figure, it is apparent that analyzing the derivative of such a function with respect to various combinations of electric field, power density, and contact size ratio allows for an interpretation of the rate of temperature increase prior to sintering to be analyzed as a function of all parameters.

To compare the initiation of sintering, a 2^{nd} degree polynomial was fit to the temperature curve for each simulation, and the 2^{nd} derivative of this polynomial was then calculated to determine the rate of temperature increase after the initial heating. The 2^{nd} derivative is a measure of the temperature during the initiation of flash sintering. The values of these derivatives were calculated for power densities ranging from 8×10^{10} W/m^3 to 8×10^{-12} W/m^3, electric fields ranging from 250 V/cm to 250,000 V/cm, and contact size ratios varying from 0 to .5.

3.3 Numerical Results

Figure 3.4 shows how the first derivative of the function changes with respect to contact size ratio, power density, and electric field. It should be noted that the first derivative is represented on a logarithmic scale. It should be noted that for the CO_2 laser running at a power of 10 W used for SLFS experiments, this corresponds to an energy

density of approximately 8×10^{11} W/m^3 in aluminum nitride powder beds. It can be seen that for both contact size ratios shown, 0 and .5, and for any given power density, the first derivative of the polynomial changes very little with varying electric field. At power densities below 1×10^{12} W/m^3 and electric fields above 10^4 V/cm, it can be seen that the first derivative increases with electric field strength. This increase appears to be linear and not logarithmic.

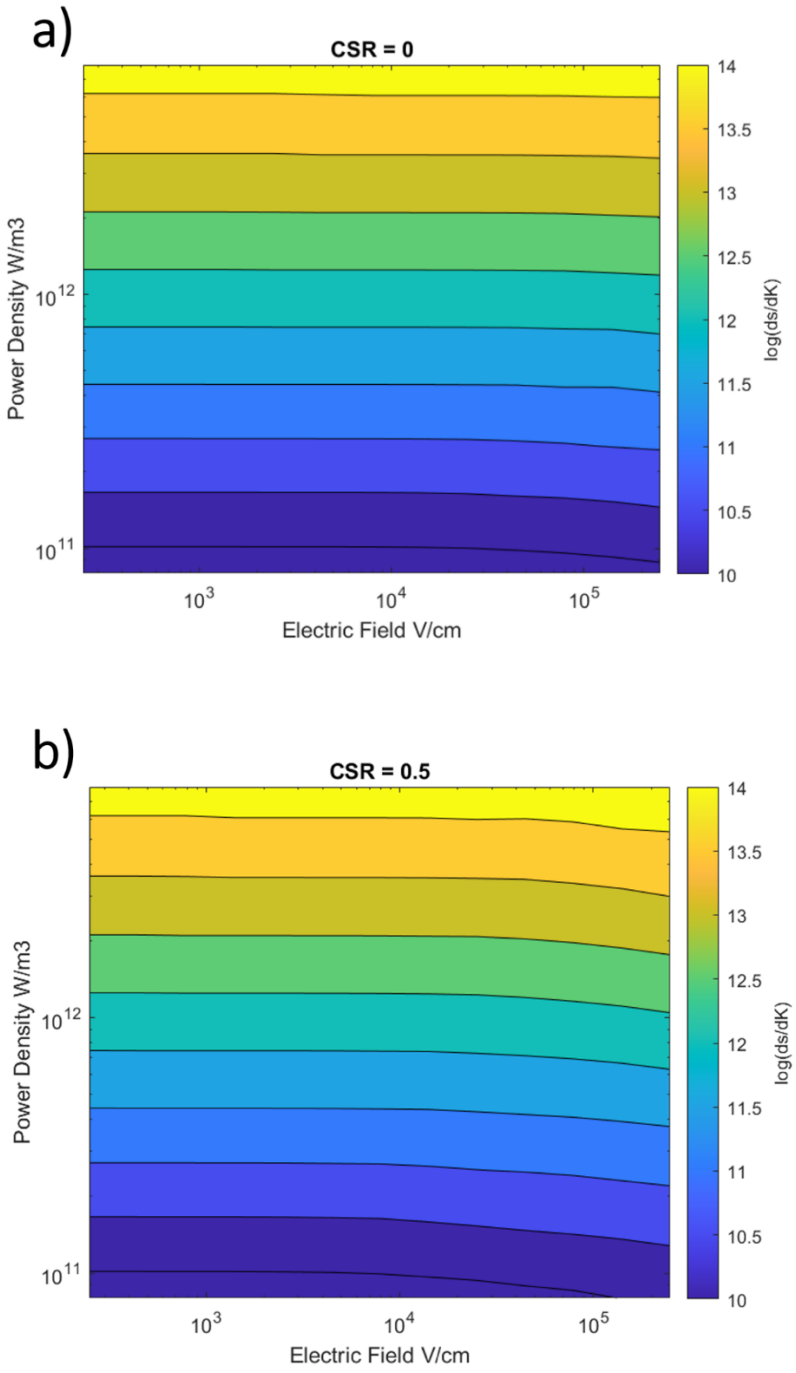

Figure 3.4: The first derivative of the temperature vs time curve as a function of power density and electric field, for contact size ratios of a) 0 and b) .5

Figure 3.4 shows the relationship between contact size ratio, power density, and electric fields from the numerical simulations. The electric fields range from 250 V/cm to a 250,000 V/cm and the power densities range from 8×10^{10} W/m^3 to 8×10^{12} W/m^3. It can be seen that with increasing contact size ratios, the rate of temperature climb increases. For each ten-fold increase in contact size ratio, as viewed by moving from Figure 3.5a to 3.5b, the second derivative of temperature increases by two decades or approximately one-hundred-fold. Thus, at a contact size ratio of 0.5, one can expect the rate of temperature increase to increase 100 times faster than at a contact size ratio of 0.05.

From Figure 3.5d, it can be seen that the log of the second derivative increases more rapidly with increasing electric field and slower with increasing power density. It should be noted that each color on the contour plot reflects two decades of second derivative growth, as indicated by the color bar on the right. The log of the second derivative starts at approximately two at an electric field of 250 V/cm and a power density of 8×10^{10} W/m^3, and rises to eighteen at an electric field of 250,000 V/cm and a power density of 8×10^{12} W/m^3. The second derivative increases by approximately four decades from a power density of 8×10^{10} W/m^3 to a power of 8×10^{12} W/m^3 for any electric field, reflecting a hundred-fold increase in the second derivative for every tenfold increase in power density. For any given power density, the second derivative increases by four decades for every one decade the electric field increase. Together, these results show that the relationship between the electric field and the temperature rate increase is 100× stronger compared to the

relationship between the power density and the temperature rate increase. This relationship holds true for all contact size ratios.

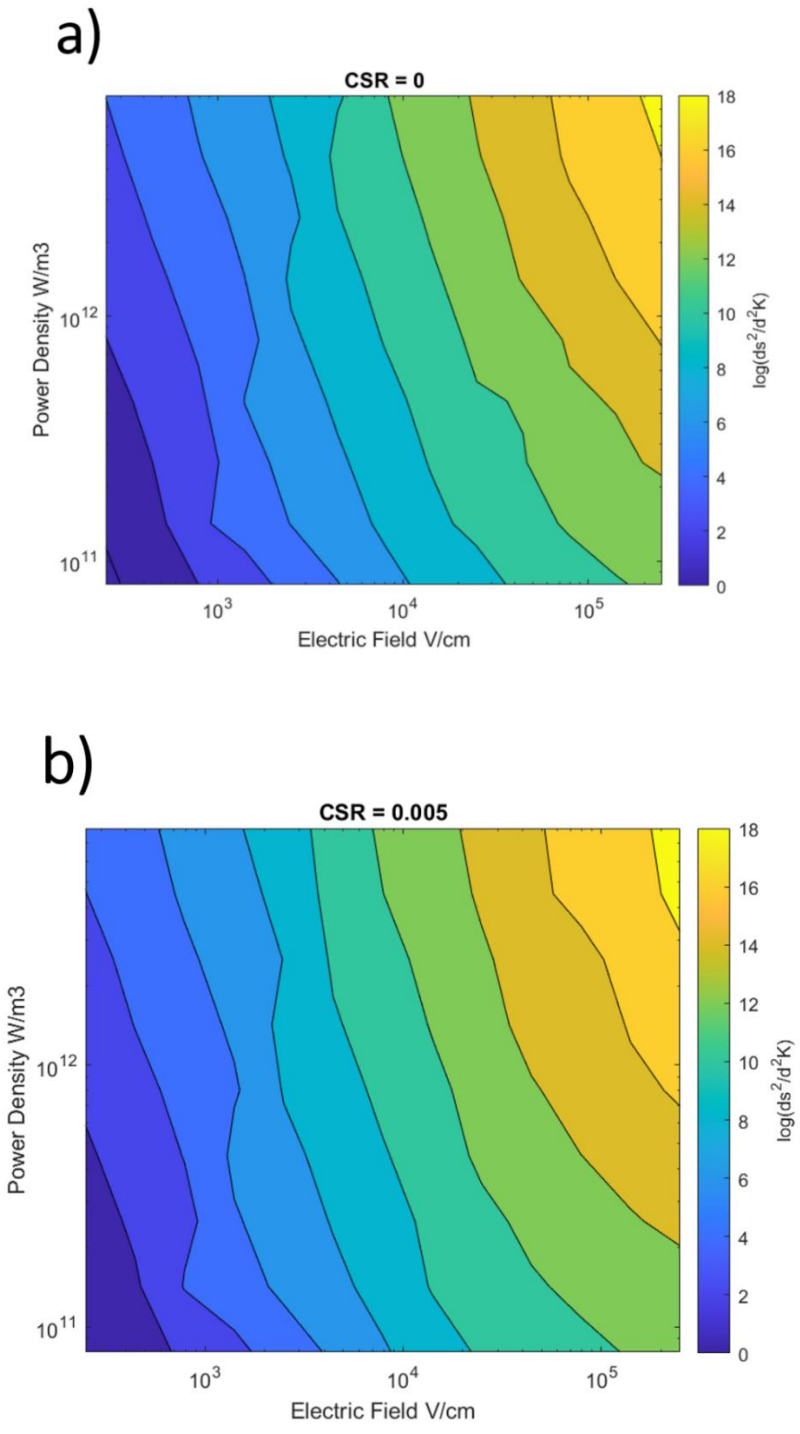

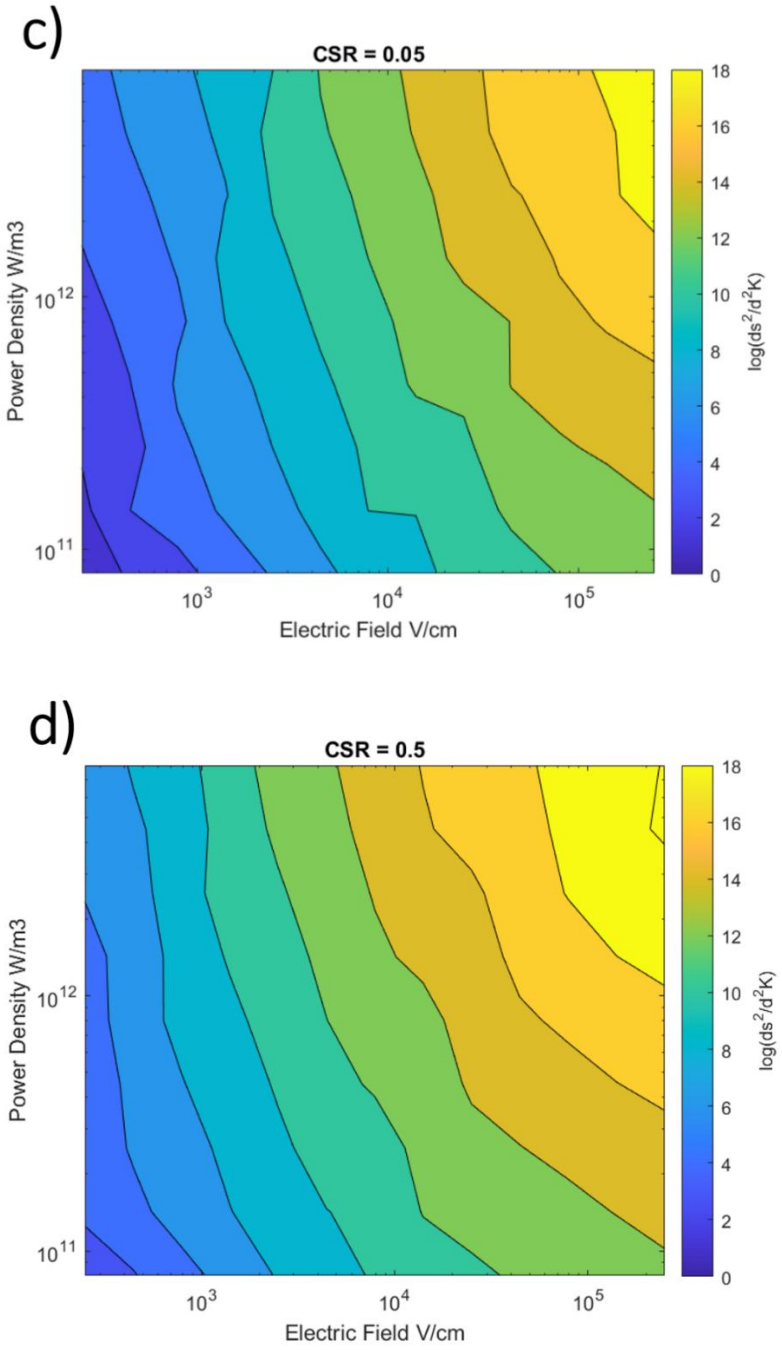

Figure 3.5: Second derivative results of various parametric conditions for contact size ratios of a) 0, b) .005, c) .05, and d) .5. Higher second derivatives indicate faster flashing and temperature climbs, note results are on a log scale.

When comparing contact size ratios, it can be seen that for every decade increase in contact size ratio, there is a two decade increase in the second derivative for any combination of electric field and power density. It should be noted that a contact size ratio of 0 is effectively an infinitely smaller than a contact size ratio of 0.005, but as with thermal conductivity, contact size ratios <<0.01 have negligible effects on material properties, as shown in Figure 2.1.

3.4 Summary

The domination of power density on the first derivative of the temperature curve as shown in Figure 3.4 is expected, as power density is introduced into the sample at a linear rate, and this alone will cause a linear increase with temperature. After a certain threshold temperature is reached, the electric field combined with increased conductivity will cause Joule heating to rapidly raise the temperature and sintering begins. At very high electric fields ($>10^4$ V/cm) the rate also increases with electric field strength, but this is likely not physically plausible because at such high fields the atmosphere experiences electrical breakdown.

Figure 3.5 highlights the effect of electric field on the temperature increase occurring from the onset of sintering. Larger second derivative terms indicate more rapid sintering and lower temperatures required before Joule heating takes over as the primary driver of the flash. It can be seen the strongest relationship exists among electric field and

the sintering rate. This is reasonable as a higher electric field will drive more current through the sample and thus cause greater Joule heating at a more rapid rate than a lower field. It is important to note however that this process does not start until the minimum threshold temperature is reached, which is primarily a function of the volumetric power density.

CHAPTER 4: CONCLUSIONS AND FUTURE WORK

Experiments showed that SLFS can be observed in aluminum nitride, as confirmed via microstructural changes. It was then shown that while laser power, scan speed, and laser power multiplied by interaction time have an effect on the initiation of flash in aluminum nitride, neither predict the onset of flash. Numerical simulations were performed to simulate the heat distributions within aluminum nitride during the onset of flash, and it was found that the minimum temperature along the scanned region predicts the onset of flash. The threshold minimum temperature required was found to be approximately 450 – 475 K.

A numerical model was then created for a parametric study of the flash sintering process as caused by Joule heating at the micro scale. A series of three aluminum nitride particles 1 μm in size were subject to various combinations of volumetric power density, contact size ratio, and electric field over time. To analyze the results of the study, the first and second derivatives of the temperature curves were analyzed. It was found that the time until the onset of flash is predominantly controlled by the volumetric power density, and that the speed at which the sintering occurs once it begins is predominantly controlled by the electric field.

The combination of continuum modeling and micro-scale modeling of SLFS has been used to develop a better understanding of the parameters that control the flash sintering process. An even greater understanding of the physics of SLFS would be possible

by extending the multi-scale modeling efforts. Multi-scale modeling would allow for the establishment of a relationship between parameters such as laser power, scan speed, and material on the continuum level to the micro-scale physics that control the flash sintering process. This may allow for the ability to control the microstructure resulting from selective laser flash sintering experiments, in addition to other events such as crack formation, by a having a thorough understanding of the physical consequences of various processing parameters.

References

1 Rahaman MN. Ceramic processing and sintering. CRC press; 2003.

2 Castro R, Van Benthem K, editors. Sintering: mechanisms of convention nanodensification and field assisted processes. Springer Science & Business Media; 2012

3 Cologna M, Prette AL, Raj R. Flash-sintering of cubic yttria-stabilized zirconia at 750° C for possible use in SOFC manufacturing. Journal of the American Ceramic Society. 2011;94(2):316-9.

4 Francis JS, Cologna M, Raj R. Particle size effects in flash sintering. Journal of the European Ceramic Society. 2012;32(12):3129-36.

5 M'Peko JC, Francis JS, Raj R. Impedance spectroscopy and dielectric properties of flash versus conventionally sintered yttria-doped zirconia electroceramics viewed at the microstructural level. Journal of the American Ceramic Society. 2013;96(12):3760-7.

6 Steil MC, Marinha D, Aman Y, Gomes JR, Kleitz M. From conventional ac flash-sintering of YSZ to hyper-flash and double flash. Journal of the European Ceramic Society. 2013;33(11):2093-101.

7 Biesuz M, Pinter L, Saunders T, Reece M, Binner J, Sglavo VM, Grasso S. Investigation of electrochemical, optical and thermal effects during flash sintering of 8YSZ. Materials. 2018;11(7):1214.

8 Todd RI, Zapata-Solvas E, Bonilla RS, Sneddon T, Wilshaw PR. Electrical characteristics of flash sintering: thermal runaway of Joule heating. Journal of the European Ceramic Society. 2015;35(6):1865-77.

9 Baraki R, Schwarz S, Guillon O. Effect of electrical field/current on sintering of fully stabilized zirconia. Journal of the American Ceramic Society. 2012;95(1):75-8.

10 Raj R. Joule heating during flash-sintering. Journal of the European Ceramic Society. 2012;32(10):2293-301.

11 Du Y, Stevenson AJ, Vernat D, Diaz M, Marinha D. Estimating Joule heating and ionic conductivity during flash sintering of 8YSZ. Journal of the European Ceramic Society. 2016;36(3):749-59.

12 Chaim R. Liquid film capillary mechanism for densification of ceramic powders during flash sintering. Materials. 2016;9(4):280.

13 Naik KS, Sglavo VM, Raj R. Flash sintering as a nucleation phenomenon and a model thereof. Journal of the European Ceramic Society. 2014;34(15):4063-7.

14 Downs, J.A., 2013. Mechanisms of flash sintering in cubic zirconia (Doctoral dissertation, University of Trento).

15 Janek J, Korte C. Electrochemical blackening of yttriastabilized zirconia â “morphological instability of the moving reaction front. Solid State Ionics. 1999;116 (3):181–195

16 Deckers J, Vleugels J, Kruth JP. Additive manufacturing of ceramics: a review. Journal of Ceramic Science and Technology. 2014;5(4):245-60.

17 Ouyang JH, Nowotny S, Richter A, Beyer E. Laser cladding of yttria partially stabilized ZrO2 (YPSZ) ceramic coatings on aluminum alloys. Ceramics international. 2001;27(1):15-24.

18 Li JF, Li L, Stott FH. Comparison of volumetric and surface heating sources in the modeling of laser melting of ceramic materials. International journal of heat and mass transfer. 2004;47(6-7):1159-74.

19 Liu ZH, Nolte JJ, Packard JI, Hilmas G, Dogan F, Leu MC. Selective laser sintering of high-density alumina ceramic parts. InProceedings of the 35th international MATADOR conference 2007 (pp. 351-354). Springer, London.

20 Himmer T, Nakagawa T, Noguchi H. Sterelithography of Ceramics. In 1997 International Solid Freeform Fabrication Symposium 1997.

21 Gonzalez JA, Mireles J, Lin Y, Wicker RB. Characterization of ceramic components fabricated using binder jetting additive manufacturing technology. Ceramics International. 2016;42(9):10559-64.

22 Lv X, Ye F, Cheng L, Fan S, Liu Y. Binder jetting of ceramics: Powders, binders, printing parameters, equipment, and post-treatment. Ceramics International. 2019.

23 Green DJ. An introduction to the mechanical properties of ceramics. Cambridge university press; 1998.

24 Jha SK, Terauds K, Lebrun JM, Raj R. Beyond flash sintering in 3 mol% yttria stabilized zirconia. Journal of the Ceramic Society of Japan. 2016;124(4):283-8.

25 Grimley CA, Prette AL, Dickey EC. Effect of boundary conditions on reduction during early stage flash sintering of YSZ. Acta Materialia. 2019;174:271-8.

26 Cologna M, Rashkova B, Raj R. Flash Sintering of Nanograin Zirconia in < 5 s at 850 degrees C. J Am Ceram Soc. 2010;93(11):3556-9.

27 Jha SK, Terauds K, Lebrun JM, Raj R. Beyond flash sintering in 3 mol % yttria stabilized zirconia. J Ceram Soc Jpn. 2016;124:283–8.

28 Yu M, Grasso S, Mckinnon R, Saunders T, Reece MJ. Review of flash sintering: materials, mechanisms and modelling. Adv Appl Ceram. 2017;116(1):24-60.

29 Shikhar K. JHA KT, Jean-Marie LEBRUN and Rishi RAJ. Beyond flash sintering in 3 mol % yttria stabilized zirconia. J Ceram Soc Jpn. 2016;124(4):P4-1-P4-.

30 Hagen, D, Beaman, JJ, Kovar, D. Selective laser flash sintering of 8-YSZ. J Am Ceram Soc. 2020; 103: 800– 808.

31 Prette AL, Cologna M, Sglavo V, Raj R. Flash-sintering of Co2MnO4 spinel for solid oxide fuel cell applications. J. Power Sources. 2011;196(4):2061-5.

32 Muccillo R, Muccillo EN. Electric field-assisted flash sintering of tin dioxide. J Eur Ceram. 2014;34(4):915-23.

33 Niu B, Zhang F, Zhang JY, et al. Ultra-fast densification of boron carbide by flash spark plasma sintering. Scr Mater. 2016;116:127–130.

34 Zapata-Solvas, E., et al. Preliminary investigation of flash sintering of SiC. J Eur Ceram. 33.13-14 (2013): 2811-2816.

35 Hagen D, Chen A, Beaman J, Kovar D, Moisture Effects on Selective Laser Flash Sintering of Yttria-Stabilized Zirconia. Proceedings of the 30th Annual International Solid Freeform Fabrication Symposium, 2019.

36 Dong Y, Chen IW. Predicting the onset of flash sintering. J Am Ceram Soc. 2015;98(8):2333-5.

37 Raftery AM, da Silva JG, Byler DD, Andersson DA, Uberuaga BP, Stanek CR, McClellan KJ. Onset conditions for flash sintering of UO2. J Nucl. 2017;493:264-70.

38 Xu RL, Muñoz Rojo M, Islam SM, Sood A, Vareskic B, Katre A, Mingo N, Goodson KE, Xing HG, Jena D, Pop E. Thermal conductivity of crystalline AlN and the influence of atomic-scale defects. J Appl Phys. 2019;126(18):185105.

39 Saxena SC, Chen SH. Thermal conductivity of nitrogen in the temperature range 350–2500 K. Mol Phys. 1975;29(5):1507-19.

40 Taylor KM, Lenie C. Some properties of aluminum nitride. J Electrochem Soc. 1960;107(4):308-14.

41 Sih SS, Barlow JW. The prediction of the emissivity and thermal conductivity of powder beds. Particul Sci Technol. 2004;22(4):427-40.

42 Cheng SC, Vachon RI. Thermal conductivity of packed beds and powder beds. Int J Heat Mass Transf. 1969;12(9):1201-6

43 Mishra AK, Aggarwal A, Kumar A, Sinha N. Identification of a suitable volumetric heat source for modelling of selective laser melting of Ti6Al4V powder using numerical and experimental validation approach. Int J Adv Manuf Tech. 2018;99(9-12):2257-70.

44 Sanders DJ. Temperature distributions produced by scanning Gaussian laser beams. Appl Opt. 1984;23(1):30-5.

45 Zavaliangos A, Laptev A. Combined macro-meso scale modeling of sintering. part i: Continuum approach. Recent Developments in Computer Modeling of Powder Metallurgy Processes. 2001;176:85.

46 Bagheri SM, Vajdi M, Moghanlou FS, Sakkaki M, Mohammadi M, Shokouhimehr M, Asl MS. Numerical modeling of heat transfer during spark plasma sintering of titanium carbide. Ceramics International. 2020;46(6):7615-24.

47 Mondalek, P., 2012. Numerical modeling of the spark plasma sintering process (Doctoral dissertation).

48 Hewitt IJ, Lacey AA, Todd RI. A mathematical model for flash sintering. Mathematical Modelling of Natural Phenomena. 2015;10(6):77-89.

49 Grasso S, Sakka Y, Rendtorff N, Hu C, Maizza G, Borodianska H, Vasylkiv O. Modeling of the temperature distribution of flash sintered zirconia. Journal of the Ceramic Society of Japan. 2011;119(1386):144-6.

50 Richards VL, Tien TY, Pehlke RD. High-temperature electrical conductivity of aluminium nitride. Journal of materials science. 1987;22(9):3385-90.